The Astrophysical Journal Supplement Series, 258:42 (19pp), 2022 February https://doi.org/10.3847/1538-4365/ac374f
© 2022. The Author(s). Published by the American Astronomical Society.
OPEN ACCESS

The Design and Integrated Performance of SPT-3G

J. A. Sobrin[1,2], A. J. Anderson[2,3], A. N. Bender[2,4], B. A. Benson[2,3,5], D. Dutcher[1,2], A. Foster[6], N. Goeckner-Wald[7,8], J. Montgomery[9], A. Nadolski[10], A. Rahlin[2,3], P. A. R. Ade[11], Z. Ahmed[8,12], E. Anderes[13], M. Archipley[10,14], J. E. Austermann[15], J. S. Avva[16], K. Aylor[17], L. Balkenhol[18], P. S. Barry[2,4], R. Basu Thakur[2,19], K. Benabed[20], F. Bianchini[7,8,18], L. E. Bleem[2,4], F. R. Bouchet[20], L. Bryant[21], K. Byrum[4], J. E. Carlstrom[1,2,4,5,21], F. W. Carter[2,4], T. W. Cecil[4], C. L. Chang[2,4,5], P. Chaubal[18], G. Chen[22], H.-M. Cho[12], T.-L. Chou[1,2], J.-F. Cliche[9], T. M. Crawford[2,5], A. Cukierman[7,8,12], C. Daley[10], T. de Haan[23], E. V. Denison[15], K. Dibert[2,5], J. Ding[24], M. A. Dobbs[9,25], W. Everett[26], C. Feng[27], K. R. Ferguson[28], J. Fu[10], S. Galli[20], A. E. Gambrel[2], R. W. Gardner[21], R. Gualtieri[4], S. Guns[16], N. Gupta[18], R. Guyser[10], N. W. Halverson[26,29], A. H. Harke-Hosemann[4,10], N. L. Harrington[16], J. W. Henning[2,4], G. C. Hilton[15], E. Hivon[20], G. P. Holder[27], W. L. Holzapfel[16], J. C. Hood[2], D. Howe[22], N. Huang[16], K. D. Irwin[7,8,12], O. B. Jeong[16], M. Jonas[3], A. Jones[22], T. S. Khaire[24], L. Knox[17], A. M. Kofman[10], M. Korman[6], D. L. Kubik[3], S. Kuhlmann[4], C.-L. Kuo[7,8,12], A. T. Lee[16,30], E. M. Leitch[2,5], A. E. Lowitz[2], C. Lu[27], S. S. Meyer[1,2,5,21], D. Michalik[22], M. Millea[16], T. Natoli[2], H. Nguyen[3], G. I. Noble[9], V. Novosad[24], Y. Omori[7,8], S. Padin[2,19], Z. Pan[1,2,4], P. Paschos[21], J. Pearson[24], C. M. Posada[24], K. Prabhu[17], W. Quan[1,2], C. L. Reichardt[18], D. Riebel[22], B. Riedel[38], M. Rouble[9], J. E. Ruhl[6], B. Saliwanchik[6,31], J. T. Sayre[26], E. Schiappucci[18], E. Shirokoff[2,5], G. Smecher[32], A. A. Stark[33], J. Stephen[21], K. T. Story[7,8], A. Suzuki[30], C. Tandoi[10], K. L. Thompson[7,8,12], B. Thorne[17], C. Tucker[11], C. Umilta[27], L. R. Vale[15], K. Vanderlinde[34,35], J. D. Vieira[10,14,27], G. Wang[4], N. Whitehorn[28,36], W. L. K. Wu[8,12], V. Yefremenko[4], K. W. Yoon[7,8,12], and M. R. Young[35]

[1] Department of Physics, University of Chicago, 5640 South Ellis Avenue, Chicago, IL 60637, USA; joshuasobrin@uchicago.edu
[2] Kavli Institute for Cosmological Physics, University of Chicago, 5640 South Ellis Avenue, Chicago, IL 60637, USA
[3] Fermi National Accelerator Laboratory, MS209, P.O. Box 500, Batavia, IL 60510, USA
[4] High-Energy Physics Division, Argonne National Laboratory, 9700 South Cass Avenue, Argonne, IL 60439, USA
[5] Department of Astronomy and Astrophysics, University of Chicago, 5640 South Ellis Avenue, Chicago, IL 60637, USA
[6] Department of Physics, Case Western Reserve University, Cleveland, OH 44106, USA
[7] Department of Physics, Stanford University, 382 Via Pueblo Mall, Stanford, CA 94305, USA
[8] Kavli Institute for Particle Astrophysics and Cosmology, Stanford University, 452 Lomita Mall, Stanford, CA 94305, USA
[9] Department of Physics and McGill Space Institute, McGill University, 3600 Rue University, Montreal, Quebec H3A 2T8, Canada
[10] Department of Astronomy, University of Illinois at Urbana-Champaign, 1002 West Green Street, Urbana, IL 61801, USA
[11] School of Physics and Astronomy, Cardiff University, Cardiff CF24 3YB, UK
[12] SLAC National Accelerator Laboratory, 2575 Sand Hill Road, Menlo Park, CA 94025, USA
[13] Department of Statistics, University of California, One Shields Avenue, Davis, CA 95616, USA
[14] Center for AstroPhysical Surveys, National Center for Supercomputing Applications, Urbana, IL 61801, USA
[15] NIST Quantum Devices Group, 325 Broadway Mailcode 817.03, Boulder, CO 80305, USA
[16] Department of Physics, University of California, Berkeley, CA 94720, USA
[17] Department of Physics & Astronomy, University of California, One Shields Avenue, Davis, CA 95616, USA
[18] School of Physics, University of Melbourne, Parkville, VIC 3010, Australia
[19] California Institute of Technology, 1200 East California Boulevard, Pasadena, CA 91125, USA
[20] Institut d'Astrophysique de Paris, UMR 7095, CNRS & Sorbonne Université, 98 bis boulevard Arago, F-75014 Paris, France
[21] Enrico Fermi Institute, University of Chicago, 5640 South Ellis Avenue, Chicago, IL 60637, USA
[22] University of Chicago, 5640 South Ellis Avenue, Chicago, IL 60637, USA
[23] High Energy Accelerator Research Organization (KEK), Tsukuba, Ibaraki 305-0801, Japan
[24] Materials Sciences Division, Argonne National Laboratory, 9700 South Cass Avenue, Argonne, IL 60439, USA
[25] Canadian Institute for Advanced Research, CIFAR Program in Gravity and the Extreme Universe, Toronto, ON, M5G 1Z8, Canada
[26] CASA, Department of Astrophysical and Planetary Sciences, University of Colorado, Boulder, CO 80309, USA
[27] Department of Physics, University of Illinois Urbana-Champaign, 1110 West Green Street, Urbana, IL 61801, USA
[28] Department of Physics and Astronomy, University of California, Los Angeles, CA 90095, USA
[29] Department of Physics, University of Colorado, Boulder, CO 80309, USA
[30] Physics Division, Lawrence Berkeley National Laboratory, Berkeley, CA 94720, USA
[31] Department of Physics, Brookhaven National Laboratory, Upton, NY 11973, USA
[32] Three-Speed Logic, Inc., Victoria, BC, V8S 3Z5, Canada
[33] Harvard-Smithsonian Center for Astrophysics, 60 Garden Street, Cambridge, MA 02138, USA
[34] Dunlap Institute for Astronomy & Astrophysics, University of Toronto, 50 St. George Street, Toronto, ON, M5S 3H4, Canada
[35] Department of Astronomy & Astrophysics, University of Toronto, 50 St. George Street, Toronto, ON, M5S 3H4, Canada
[36] Department of Physics and Astronomy, Michigan State University, East Lansing, MI 48824, USA
Received 2021 June 18; revised 2021 October 18; accepted 2021 November 5; published 2022 February 9

Abstract

SPT-3G is the third survey receiver operating on the South Pole Telescope dedicated to high-resolution observations of the cosmic microwave background (CMB). Sensitive measurements of the temperature and polarization anisotropies of the CMB provide a powerful data set for constraining cosmology. Additionally, CMB

Original content from this work may be used under the terms of the Creative Commons Attribution 4.0 licence. Any further distribution of this work must maintain attribution to the author(s) and the title of the work, journal citation and DOI.

surveys with arcminute-scale resolution are capable of detecting galaxy clusters, millimeter-wave bright galaxies, and a variety of transient phenomena. The SPT-3G instrument provides a significant improvement in mapping speed over its predecessors, SPT-SZ and SPTpol. The broadband optics design of the instrument achieves a 430 mm diameter image plane across observing bands of 95, 150, and 220 GHz, with 1.2′ FWHM beam response at 150 GHz. In the receiver, this image plane is populated with 2690 dual-polarization, trichroic pixels (∼16,000 detectors) read out using a 68× digital frequency-domain multiplexing readout system. In 2018, SPT-3G began a multiyear survey of 1500 deg^2 of the southern sky. We summarize the unique optical, cryogenic, detector, and readout technologies employed in SPT-3G, and we report on the integrated performance of the instrument.

Unified Astronomy Thesaurus concepts: Cosmic microwave background radiation (322); Astronomical instrumentation (799); Polarimeters (1277)

1. Introduction

Measurements of the cosmic microwave background (CMB) have been instrumental to the development of ΛCDM, the standard model of the composition, structure, and evolution of our universe. Satellite experiments have measured the CMB temperature anisotropy to the cosmic-variance limit at angular multipoles $\ell \lesssim 1600$ (Hinshaw et al. 2013; Planck Collaboration et al. 2020); and high-resolution, ground-based experiments have extended these measurements to arcminute scales ($\ell \lesssim 10{,}000$) (Choi et al. 2020; Reichardt et al. 2021), providing precise measurements of the base ΛCDM model parameters. Extracting further information from the CMB at cosmic-variance dominated scales requires measurements of the polarization anisotropy, which provide additional statistical power to constrain cosmological parameters, as well as a unique sensitivity to gravitational waves produced during inflation in the early universe.

The polarization of the CMB can be decomposed into *E*-modes and *B*-modes, which correspond to the curl-free and divergence-free components of the polarization field, respectively. *E*-modes are created from quadrupole temperature anisotropies during the epoch of last scattering (Hu & White 1997). Precision measurements of *E*-mode polarization will continue to improve constraints on the physics parameters sensitive to the damping tail of the CMB and will serve as a powerful consistency test of the ΛCDM model (Galli et al. 2014). *B*-modes are generated by gravitational lensing of primordial CMB *E*-modes, galactic and extragalactic emission, and primordial gravitational waves produced during inflation (Kamionkowski et al. 1997; Zaldarriaga & Seljak 1997). Distinguishing lensed *B*-modes and foregrounds from primordial *B*-modes requires an instrument with a combination of low noise-equivalent temperature, arcminute-scale resolution, and broad frequency coverage (Abazajian et al. 2016; Kamionkowski & Kovetz 2016; BICEP/Keck Collaboration et al. 2021).

Low-noise maps of the microwave sky with arcminute-scale resolution enable a broad range of cosmology and astrophysics research beyond the CMB temperature and polarization power spectra. Measurements of the lensing-potential power spectrum (Wu et al. 2019) provide an additional way to further constrain ΛCDM model parameters and extension models (Sherwin et al. 2017; Bianchini et al. 2020a). Massive clusters of galaxies can be detected via the Sunyaev–Zeldovich effect, enabling the creation of mass-limited catalogs of clusters, completely out to the redshifts at which they are first formed (Huang et al. 2020; Hilton et al. 2021). These cluster samples provide constraints on cosmological parameters independent of those from the primary CMB (Hasselfield et al. 2013; Planck Collaboration et al. 2016b; Bocquet et al. 2019). High-resolution CMB maps also provide a rich sample of emissive point sources, including active galactic nuclei and high-redshift dusty galaxies (Planck Collaboration et al. 2016c; Everett et al. 2020; Gralla et al. 2020). In addition, time-domain analyses of CMB data monitor the sky for millimeter-wavelength transient sources, and CMB surveys are now producing catalogs of strongly flaring transients (Whitehorn et al. 2016; Naess et al. 2021; Guns et al. 2021). Dedicated analyses of CMB maps are also capable of probing exotic, beyond-the-Standard-Model physics. For example, searches for both static and time-varying birefringence can constrain extensions of the Standard Model involving new axion-like particles (BICEP2 Collaboration et al. 2017; Bianchini et al. 2020b; Namikawa et al. 2020; BICEP/Keck et al. 2021).

In this paper, we describe an instrument designed to perform these measurements: SPT-3G, the third-generation survey receiver installed on the South Pole Telescope (SPT). The SPT is a 10 m telescope located at the Amundsen–Scott South Pole Station in Antarctica and optimized to survey the CMB at millimeter wavelengths (Padin et al. 2008; Carlstrom et al. 2011). The South Pole provides an ideal site for millimeter-wave observations due to its altitude (2835 m) and exceptionally low precipitable water vapor (Radford & Holdaway 1998; Radford 2011). Furthermore, the absence of a 24 hr day–night cycle provides relatively stable, low-noise atmospheric conditions and minimal needs for Sun-avoidance measures. The survey receiver exploits the telescope's large primary aperture, using ∼16,000 polarization-sensitive detectors to provide arcminute-scale resolution maps in three observing bands located in the atmospheric transmission windows at 95, 150, and 220 GHz. The main SPT-3G survey covers a 1500 deg^2 area of southern sky that overlaps the survey of the BICEP3/BICEP Array experiment (Moncelsi et al. 2020), which has lower resolution and is optimized to detect degree-scale primordial *B*-modes. The order-of-magnitude increase in detectors in SPT-3G—relative to its predecessor instrument, SPTpol (Austermann et al. 2012)—is made possible by leveraging dual-polarization trichroic pixels, a readout system capable of higher multiplexing factors, and a wider throughput telescope design. We detail these advances and the integrated, on-sky performance of the SPT-3G instrument in this work.

The organization of this paper is as follows: Section 2 discusses the optics design, cold-refractive elements, and antireflection (AR) strategies; Section 3 describes the design and performance of the cryogenics system, level of optical loading on the detectors, and sub-kelvin assembly; Section 4 covers the design, fabrication, and properties of the detectors; Section 5 details the readout system, with discussions on noise characterization, operable detector yield, detector crosstalk, and data acquisition (DAQ); Section 6 provides an overview of the SPT-3G survey footprints and observing strategy, including a

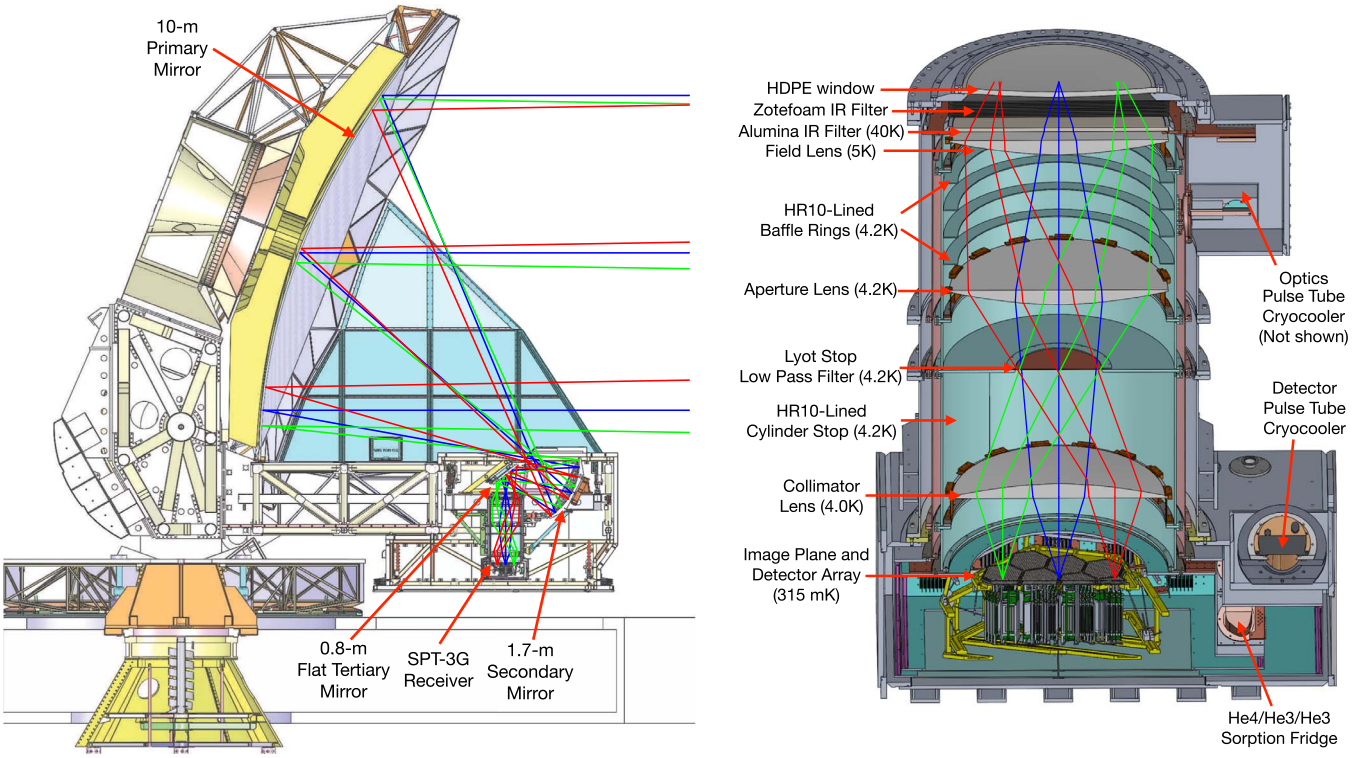

Figure 1. Left: ray trace of the SPT optics design overlaid on a cross-sectional view of the telescope and receiver. The secondary mirror, tertiary mirror, and receiver are mounted on an optics bench and housed inside a temperature-controlled cabin that moves with the telescope during observations. Reflected light from the primary mirror passes through an environmental window (6.35 mm thick HD-30 Zotefoam) on the roof of the cabin. Right: cross-sectional view of the SPT-3G receiver with ray trace overlaid. Components of the optics and cryogenics systems are labeled, with typical operating temperatures noted in parentheses.

description of calibration observations and relative-calibration procedure; and Section 7 addresses the integrated, on-sky performance of the SPT-3G instrument, including measurements of its optical efficiency, spectral response, beam response, sensitivity, and polarization calibration.

2. Optics

The optics design for SPT-3G aims to maximize the throughput and efficiency of the telescope system while minimizing aberrations, reflections, and scattering. An annotated illustration of the system is shown in Figure 1.

For SPT-3G, an off-axis Gregorian design is used to couple the 10 m diameter primary mirror of the SPT to a new 1.7 m ellipsoidal secondary (Stark 2018) and 0.8 m diameter flat tertiary mirror. A set of refractive optics inside the SPT-3G receiver reimages the Gregorian focus onto a flat image plane where the detectors are located. The primary mirror is underilluminated to shield against signals from ground emission, sidelobe pickup, and stray light within the cabin and receiver through the use of a 0.28 m diameter Lyot stop, inside the receiver, which reduces the primary illumination from 10 m diameter to 8 m diameter. The secondary mirror, tertiary mirror, and receiver are mounted on a movable optics bench that can be adjusted relative to the primary mirror to optimize the focus quality. The optics design uses pixel sizes of $1.12/1.75/2.62$ $F\lambda$ at $95/150/220$ GHz.[37] In addition to arcminute-scale resolution, this design results in predicted Strehl ratios greater than 0.98 for the detectors across all three observing bands over the entire 430 mm diameter image plane and diffraction-limited performance over the 1.88° diameter field of view. Light enters the receiver through a 685 mm diameter vacuum window made of 30 mm thick high-density polyethylene (HDPE). The AR-coating of the window consists of triangular grooves directly machined into the window surfaces, cut orthogonally on both sides to minimize birefringence and cross-polarization effects (Schroder et al. 2016). The design of the grooves is based on Raguin & Morris (1993), with groove spacing of 0.652 mm and groove depth of 1.321 mm, which we calculate to result in per-surface reflection of $<0.3\%$ over the 95 GHz observing band, and $<0.1\%$ over the 150 GHz and 220 GHz observing bands. Beyond the window, a set of three sintered, polycrystalline, Coorstek AD-995 aluminum oxide (alumina) lenses comprises the refractive optics chain. Each lens is a 0.72 m diameter, plano-convex, sixth-order asphere with center thickness between 54 and 69 mm. Laboratory measurements of Coorstek AD-995 samples indicate an index of refraction of $n = 3.089$ and a loss tangent of $\tan\delta = 3 \times 10^{-4}$ at 77 K (Nadolski et al. 2020).

At each pixel of the image plane, an extended hemispherical lens (lenslet) couples radiation to a polarization-sensitive sinuous antenna (Section 4.1). Lenslets consist of 5 mm diameter alumina hemispheres epoxied to circular depressions in a silicon *lenslet wafer* using thin fillets of Stycast 1266 (Nadolski 2020). Each array of lenslets is clamped to a silicon wafer containing the antennas and detectors. The two wafers are positioned relative to each other with an accuracy of <10 μm using alignment marks visible with an infrared (IR) microscope.

[37] $F\lambda$ is defined as the product of the optics design's f-number and the wavelength of light.

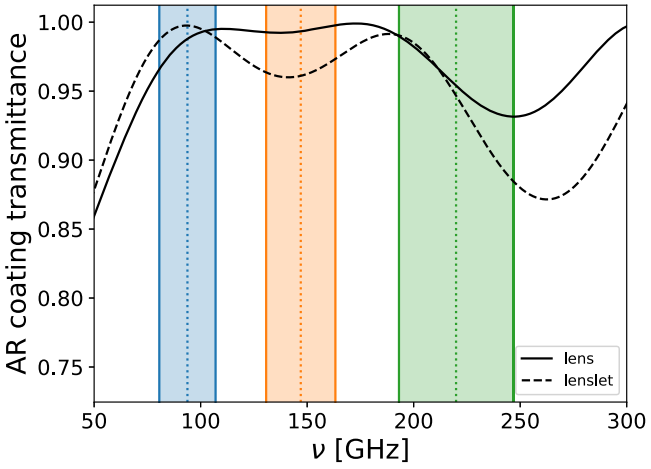

Figure 2. Predicted transmission through a single AR-coated alumina surface, for both lens (solid line) and lenslet (dashed line) prescriptions. The predictions use laboratory-measured values of dielectric constants and material thicknesses for the constituent materials. The shaded regions denote the SPT-3G observing bands, centered at 95, 150, and 220 GHz (Section 7.3).

Broadband AR coatings are used to minimize reflective losses at the alumina lenslets, lenses, and alumina IR filter (Section 3) across the 80–250 GHz range. Separate prescriptions utilizing three distinct layers of polytetrafluoroethylene-based dielectrics were developed for both the large-format monolithic elements and the densely packed lenslet arrays. A complete description and characterization of these AR coatings can be found in Nadolski et al. (2020). Figure 2 shows the expected transmission at lens and lenslet surfaces assuming the measured material properties. At the alumina IR filter and lens surfaces, we expect an average reflection of 1.1/0.6/5.1 percent per surface across the 95/150/220 GHz observing band. Similarly, at the lenslet surface, we expect an average reflection of 0.6/3.4/6.1 percent across the 95/150/220 GHz observing band. Absorption in the AR coatings is negligible compared to the level of attenuation through the bulk alumina and reflective loss at each surface.

To further control stray light inside the receiver, Eccosorb HR-10 is attached using Stycast adhesive to the innermost aluminum surfaces, both between the collimator lens and Lyot stop and between the Lyot stop and field lens. HR-10 is flexible, thereby conforming to the aluminum surfaces and, more importantly, has minimal reflection ($\lesssim$2%) even at high angles of incidence ($\lesssim$80°) at millimeter wavelengths (Staniszewski 2010). In addition, a set of four baffle rings covered with HR-10 is positioned between the aperture and field lens to provide surfaces at near-normal incidence to further improve the absorption of stray light.

3. Cryogenics

The SPT-3G receiver is cryogenically cooled to minimize the instrument's intrinsic in-band thermal emission onto the detector array, as well as to provide a sufficiently cold environment for the detector and readout systems to effectively operate. In addition, several low-pass optical filters are employed to shield downstream instrument elements and the detector array from submillimeter-wavelength, out-of-band power.

The receiver—shown in Figure 1—is functionally separated into an optics and detector cryostat, both cooled by the dedicated Cryomech PT-415 cryocoolers (PTCs) while sharing a single vacuum space. The optics cryostat securely positions and cools the IR blocking filters, lenses, and Lyot stop. The detector cryostat houses the ten detector modules and cryogenic components of the associated readout electronics. Before the initial cooldown from room temperature, the receiver is pumped out to ∼millitorr pressure over ∼24 hr, after which the two PTCs are turned on. From that point, the receiver needs roughly seven days to reach its base temperature of ∼3 K.

Past the window, a combination of filters minimizes the transmission of IR radiation, which would raise the base temperatures of the optics elements. Mounted to the flange holding the vacuum window is a set of ten 3.175 mm thick HD-30 Zotefoam sheets, separated by thermally-insulating G-10 spacers. The Zotefoam sheets are transmissive at millimeter wavelengths and absorptive at IR wavelengths, thereby acting as a multilayered IR-absorptive filter (Choi et al. 2013; Kang et al. 2018). We estimate this first filter assembly attenuates any incident IR power through and from the window by a factor of ∼10, while attenuating the CMB signal by <1%. Beneath the Zotefoam-filter assembly, and thermally connected to the first stage of the optics PTC, is a 15 mm thick, 720 mm diameter disk of alumina that provides additional IR filtering. During typical winter observations, this alumina IR filter equilibrates to a temperature of 40 K, with a gradient of <1 K across the filter, thereby contributing a radiative load of <0.1 W on the first lens. A final metal-mesh low-pass filter (LPF), with a cutoff of 270 GHz, mounted at the Lyot stop further suppresses power above the observing bands of the detectors (Ade et al. 2006).

The thermal stages, connected to the first- and second-stage cold-heads of the PTCs (henceforth referred to as the 50K stage and 4K stage, respectively), are mechanically supported and thermally-isolated by a circular truss assembly of G-10 tubes. The individual tubes are 6.35 mm in outer diameter, with 0.76 mm wall thickness, and have ∼25 mm length between stages.

The base temperatures of elements within the receiver are limited by the thermal loading on the PTCs. To mitigate the development of significant thermal gradients across the receiver, a combination of multilayered insulation (MLI), high thermal-conductivity material choices, and IR-filtering techniques are employed, as described in Sobrin et al. (2018). Elevated base temperatures within the receiver would contribute to an increased extraneous optical power on the detectors, a lower observing efficiency, and a deteriorated SQUID amplifier performance (Section 5). Table 1 shows the predicted thermal power on both stages from a combination of heat sources. Radiative sources include out-of-band (primarily IR) thermal power coming through and from the vacuum window and alumina IR filter, along with radiative heat transfer between different temperature-stage cryostat shells. Conductive sources include the readout wiring, aluminzed-mylar radio-frequency shielding (RF shielding), and G-10 truss assemblies mechanically supporting the radiation shields and alumina IR filter. The measured temperatures of the PTC cold-heads provide a rough probe of the actual heat load on each thermal stage, from which we infer lower-than-expected and higher-than-expected loading on the 50K and 4K stage, respectively. Given the lower optics PTC 50K cold-head temperature, it is possible that the vacuum window equilibrates to a colder-than-expected temperature during normal operations, thereby emitting less thermal radiation to the alumina IR filter through

Table 1
Thermal Loading on the SPT-3G 50K and 4K Stages

Source	50K Stage (W)	4K Stage (mW)
Vacuum Window	8.8	60
Radiation	18.1	90
RF Shielding	1.5	30
Readout Wiring	2.9	130
G-10 Supports	2.1	80
Total Predicted Load	33.4	390
PTC Cold-head Temp.	29/35 K	3.5/3.1 K
Total Inferred Load	25	800

Note. The values for each source are calculated for the fully-integrated receiver. Cold-head temperatures are listed for the optics and detector PTCs, respectively. Laboratory load-curve measurements are used to infer the actual heat load on each stage from the PTC temperatures.

the Zotefoam-filter assembly. It is also possible that the MLI surrounding the entire 50K stage is slightly more effective than predicted. Considering the higher optics PTC 4K cold-head temperature, we suspect higher-than-expected radiative power on the first alumina lens, either through the alumina IR filter or through unanticipated radiative coupling to room-temperature elements at the top end of the optics cryostat. Nonetheless, the level of additional loading on the 4K stage is not high enough to noticeably affect the helium condensation (and therefore, performance) of the sub-kelvin sorption refrigerator (Section 3.1), or dramatically affect the optical loading on the detectors. The warmest SQUID amplifiers in the receiver operate at 3.9 K, a temperature that does not result in significantly elevated overall system noise.

Each element of the optics system transmits in-band light with imperfect efficiency and contributes its own extraneous optical power onto the detectors through thermal emission. The instrument's sensitivity to the CMB depends on both its cumulative optical efficiency and its optical loading onto the detectors, details of which are summarized in Table 2. Each element's efficiency is determined by both the level of reflection at the surfaces and the level of absorption through the bulk material (which is a function of material loss tangent and thickness). Extraneous optical power from the instrument is minimized by cryogenically cooling most elements. In addition, the cold Lyot stop and absorptive baffling define the outer edges of the beams and terminate grazing reflections to minimize the level of diffusive ray scattering onto hot, emissive surfaces. Through a comparison of saturation powers of optical and dark detectors (Dutcher et al. 2018), we find that the optical loading on the detectors is reasonably consistent with the predicted values in Table 2. The instrument's optical efficiency is further explored in Section 7.2.

3.1. Sub-kelvin Assembly

The detector array must be held at an equilibrium temperature of ∼300 mK to operate, which is achieved with a custom closed-cycle ^{3}He–^{3}He–^{4}He sorption refrigerator fabricated by Chase Research Cryogenics (Bhatia et al. 2000). The refrigerator's ultra-cold cooler (UC) is capable of reaching a base temperature of 265 mK under a 4 μW load, and is bolstered by an intermediate cooler (IC) and buffer cooler (1K), which reach 330 mK and 980 mK under 20 μW and 100 μW loads, respectively.

The sub-kelvin thermal stages thermally isolate and position the 22 kg detector array at the image plane of the optics system, while maintaining sufficiently cold and stable temperatures by contributing minimal thermal loads on the sorption refrigerator. Graphlite, a proprietary carbon-fiber reinforced polymer,[38] is used in a truss configuration to robustly position and support the individual thermal stages. Graphlite has been previously measured to have a thermal conductivity of 1.8 m $\mathrm{Wm^{-1}\,K^{-1}}$ at sub-kelvin temperatures (Runyan & Jones 2008), a value we found to be consistent with our own laboratory measurements. Although the inherent thermal conductivity of Graphlite below 4 K is an order-of-magnitude higher than other commercially available plastics, such as Vespel, its superior strength and stiffness provides a better balance of strength and conductivity in this temperature range. The Graphlite rods are sanded on their ends, concentrically positioned in tapped holes of aluminum blocks, and bonded using 3M Scotch-Weld Epoxy Adhesive 2216 Gray. Prototype joints were tension-tested at liquid nitrogen temperatures, and consistently survived forces in excess of 7000 N.

The detector modules are mounted to the UC stage, which reaches a base temperature of 285 mK. Attached to the back of each detector module is a set of circuit boards that hold the lithographed inductor–capacitor (LC) chips (Section 5). These boards (∼300 mK) are electrically connected to the SQUID amplifiers (∼4 K) via low thermal-conductance NbTi striplines, which are heat-sunk to the IC and 1K thermal stages. This strategy reduces conductive loading at the UC stage by shunting most of the wiring heat to the intermediate thermal stages, which have more cooling power. An additional source of conductive heat on the 1K and UC stages comes through a continuous sheet of aluminized mylar spanning the gap between the 4K and UC stages. This sheet is a codominant source of loading on the UC stage, but provides an important part of the electromagnetic interference (EMI) shielding around the sensitive readout electronics in the detector cryostat. In combination with a similar sheet between 300K and 4K in the optics cryostat, the aluminized mylar acts as a continuous Faraday cage, shielding the detectors and cryogenic readout electronics from EMI entering primarily through the vacuum window. The estimated heat loads on each thermal stage are outlined in Table 3.

This current version of the sub-kelvin assembly, a photo of which is shown in Figure 3, was installed in 2018 December. An earlier version of the assembly was insufficiently stiff and sensitive to vibrations induced by the telescope's motion, resulting in microphonic heating of the UC stage and excess low-frequency noise in the detectors. To mitigate these effects, the currently fielded assembly was designed to increase the frequency of the lowest resonant modes while maintaining an acceptable level of conductive heat load between the thermal stages. Whereas the earlier version utilized oxygen-free high thermal-conductivity (OFHC) copper at each thermal stage to minimize thermal gradients, the current design uses thicker gold-plated aluminum at each thermal stage to improve the assembly's stiffness. Thicker Graphlite struts are now used between the thermal stages, and several design features were added to better account for differential thermal contraction

[38] https://goodwinds.com/product-category/carbon-fiberglass/carbon/solid-round/

Table 2
Predicted Optical Loading and Efficiency for SPT-3G

Source	Temperature (K)	$P_{\rm optical}$ (pW) 95/150/220	Transmission/Efficiency (η) 95/150/220
Pixel and Lenslet	0.3	<0.01 across bands	0.81/0.83/0.73
Lyot Stop	4.2	0.16/0.10/0.01	0.56/0.82/0.96
Metal-mesh LPF	4.2	0.02/0.03/0.02	0.94/0.94/0.94
3 Lenses	4–5	0.13/0.19/0.21	0.75/0.71/0.46
Alumina IR Filter	40	0.24/0.49/0.96	0.95/0.95/0.85
Zotefoam-filter Assembly	∼150–280	0.03/0.15/0.26	1.00/1.00/0.99
Vacuum Window	280	0.73/2.59/2.50	0.98/0.96/0.95
Cabin Environmental Window	240	0.01/0.03/0.03	>0.99 across bands
Telescope Mirrors	∼250–280	0.45/1.36/1.31	0.99/0.98/0.97
Total Instrument		1.78/4.94/5.30	0.29/0.41/0.23
(excluding stop efficiency)		...	0.52/0.50/0.24
Atmosphere	230	1.69/2.83/1.91	0.93/0.95/0.95
CMB	2.7	0.11/0.13/0.03	...
Total		3.58/7.90/7.24	0.27/0.38/0.22

Note. For each element, the optical-power contributions are dependent on the element's temperature, emissivity, reflectivity, scattering, and absorption. Each element's efficiency is defined as the band-averaged efficiency, averaged over the expected bandpass of the in-line filters on the detector wafers (Section 4.1). The efficiency values for the pixel & lenslet are based on laboratory measurements using a tunable blackbody radiative source to illuminate SPT-3G pixels (Anderson et al. 2020). The Lyot stop efficiencies are the fractions of power that propagate through the stop, estimated from time-reverse Gaussian propagation analyses of the beams at the lenslet; therefore, the stop does not contribute true loss to the system, and we additionally include the total-instrument efficiency without it. Transmission through bulk elements is calculated assuming an attenuation of $e^{-\delta kz}$, where δ refers to the loss tangent of the material, k refers to the wavenumber, and z refers to the thickness of the element. Loss at the telescope mirrors is dominated by the panel gaps in the primary mirror (∼1% of the total primary area; Carlstrom et al. 2011), and the finite conductivity of the aluminum used for all three mirrors. Atmospheric loading is estimated assuming 50% median precipitable water vapor in the six month period between June through November at the South Pole, using the AM code (Paine 2019). The table provides the predicted efficiency of any detector to a single polarization.

Table 3
Thermal Loading on the SPT-3G Sub-kelvin Stages

Source	1K Stage (μW)	IC Stage (μW)	UC Stage (μW)
Graphlite Struts	39	2.1	0.06
Wiring	11	3.3	0.48
RF Shielding	21	...	0.42
Radiation	0	0	0.16
Total Predicted Load	71	5.4	1.12
Cold-head Temp	∼1 K	312 mK	268 mK
Total Inferred Load	∼100	10	4.0

Note. The RF shielding bridges directly between the 1K to UC stages, and does not contribute to the IC stage loading. Radiative loads are expected to be negligible, except at the UC stage, where we expect the detector array to absorb a nonnegligible amount of thermal radiation from its 4 K surroundings. Load curves provided by Chase Cryogenics are used to infer the actual heat load on each stage from the measured cold-head temperatures. We believe the discrepancy between prediction and measurement at the IC and UC stages is caused by thermal gradients across the 1K and IC stages exacerbating the conductive loads on the IC and UC stages, respectively.

throughout the assembly. Compared to earlier versions, the current design has a higher total heat capacity and level of heat transfer between thermal stages, thereby decreasing our overall observing efficiency by a few percent. However, the current version decreases the mass of the total sub-kelvin assembly by 20%, and improves the overall stiffness of the assembly by a factor of 2. We measured the vibrational modes of the assembly and found the lowest mode to be above 50 Hz, consistent with predictions from SolidWorks simulations and well above the expected resonance frequencies of the telescope and optics bench. Since the current assembly was installed in 2018, heating of the detector array and excess detector noise due to the telescope vibrations are negligible.

During observations, the UC stage is held at 305 mK (∼20 mK above the lowest achievable temperature) using a proportional-integral-derivative controller that adjusts a sorption-pump heater in the refrigerator to control cooling power. Doing so reduces temperature fluctuations of the detector array to $\lesssim$0.1 mK, slightly improving the hold-time of the refrigerator while negligibly impacting detector performance. The refrigerator is capable of maintaining the detector modules at this operating temperature for a total of 17 hr before needing to be recycled, which sets a limit on the maximum observing efficiency to ∼80 %. Though the refrigerator is designed to support the predicted heat loads for periods of over 72 hr, the achieved hold-time is reduced primarily by two issues. First, the assembly's large heat capacity requires a significant portion of the refrigerator's finite cooling capacity per cycle to be used in cooling the detector array to base temperature from ∼3 K. Second, given the elevated operating temperatures of the refrigerator IC and UC coolers, we believe that larger-than-expected thermal gradients exist on the 1K and IC stages. Such gradients would be responsible for larger temperature differentials through conductive components between the thermal stages (e.g., NbTi striplines), leading to higher conductive loads. This latter issue could be reduced by adding better conductive heat paths across the thermal stages to mitigate gradients, thereby reducing the heat load (and required cooling power) by a factor of ∼2 at each stage. Doing so could potentially increase the time between fridge cycles by ∼75%,

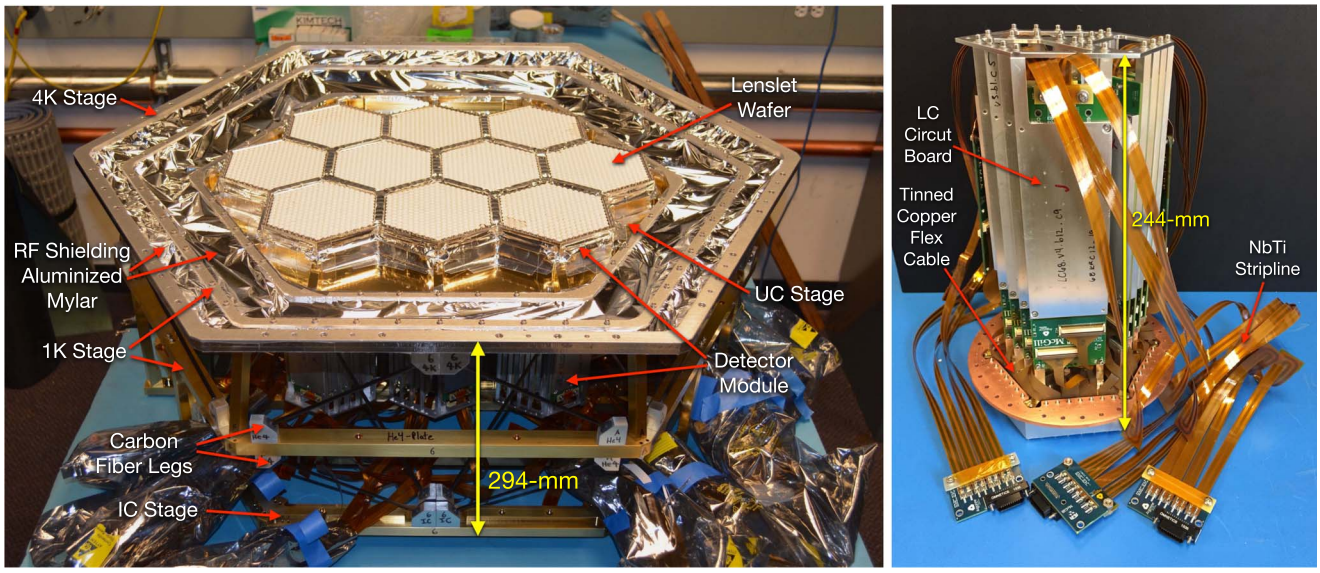

Figure 3. Left: picture of the SPT-3G detector array (consisting of 10 detector modules) and supporting sub-kelvin architecture. The thermal stages are mechanically supported by a Graphlite truss structure that stands off the UC, IC, and 1K stages from a mounting ring at 4K. Each stage is machined from aluminum alloy 6061 and gold-plated to promote thermal conductivity across the components and between interfaces. The thermal stages are coupled to the sorption refrigerator using pressure-bonded annealed OFHC braided copper straps (Sobrin et al. 2018). Right: picture of a SPT-3G detector module. Each module contains a lenslet array, detector wafer, and 12 LC readout boards. In the picture, the lenslet array is downward facing and hidden by a protective cover. The lenslet array and detector wafer are clamped together in an invar frame, and mounted to a backplate containing an Eccosorb AN-72 absorber. The absorber-covered backplate controls the response of the pixels, and also provides a mounting plate for the LC readout boards. Wire-bonded to the detector wafer are flexible cables with tinned-copper traces, which connect to the LC readout boards. Low-thermal-conductance NbTi striplines connect the LC boards to SQUID amplifiers at 4K.

but this would only increase the overall, already high, observing efficiency by a few percent.

4. Detectors

The SPT-3G detector array includes 10 detector wafers, with each wafer containing 269 trichroic pixels. Within each pixel, a broadband dual-polarized antenna couples to transition-edge sensor (TES) bolometers via Nb microstrip transmission lines (Figure 4). The signal from the antenna passes through the in-line band-defining filters before being transmitted to the respective detectors. This general pixel architecture was developed at UC Berkeley for the POLARBEAR-2/Simons Array (Suzuki et al. 2016), and is also planned for use in the Simons Observatory (Galitzki et al. 2018) and LiteBIRD (Suzuki et al. 2018) experiments.

4.1. Pixel Design

At the center of each pixel is a sinuous antenna (O'Brient et al. 2010), a type of log-periodic antenna that has several desirable properties, including dual linear polarization, planar geometry that allows for simple lithographic fabrication, low cross-polarization, and broadband response with nearly frequency-independent input impedance.

Sinuous antennas exhibit a periodic variation of polarization angle with frequency, or *polarization wobble*. Ansys HFSS simulations of this antenna design show polarization wobble with an amplitude of $\pm 5^\circ$ (Edwards et al. 2012). To reduce bias in the polarized maps, an equal number of mirror-image antennas are included on each wafer, such that the biases induced by the left-handed and right-handed wobbles cancel out on average. In addition to the mirror-image antennas, half of the antennas on each wafer are rotated by 45° to evenly sample the Stokes Q and U parameters.

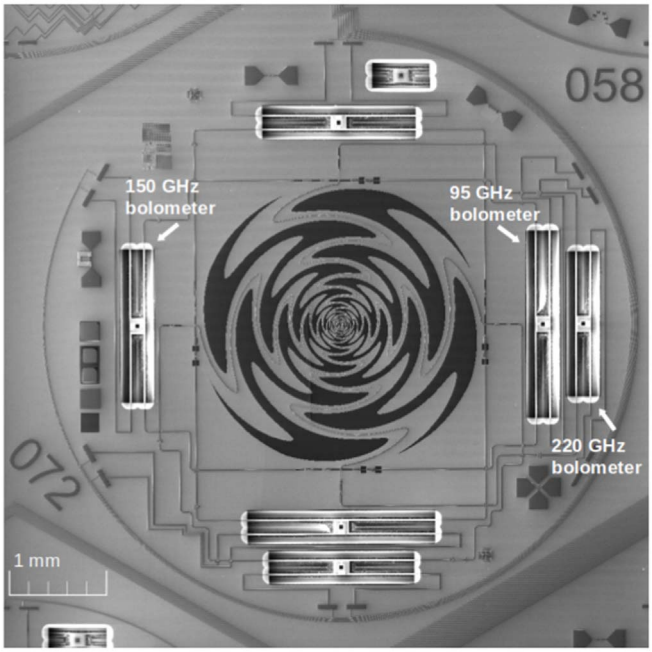

Figure 4. Scanning electron microscope micrograph of an SPT-3G pixel, showing the sinuous antenna at the center surrounded by six TES bolometers as well as various test structures. The bolometers corresponding to one polarization state have been labeled with their respective observing bands.

The signal from each antenna couples to a microstrip transmission line that lies atop the metalized antenna arms. An in-line triplexer circuit (Figure 5) separates the broadband signal from the antenna into the three observing bands, centered at approximately 95, 150, and 220 GHz. The triplexer (Suzuki et al. 2012) consists of quasi-lumped-element filters, in which sections of microstrips are removed or formed

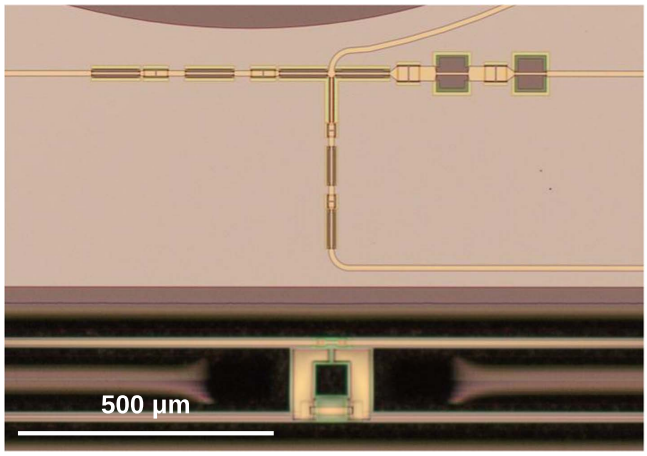

Figure 5. Zoom-in on the SPT-3G pixel, showing a triplexer filter circuit (top) and the bolometer island (bottom). On the bolometer island, the termination resistor is located at the top while the TES is at the bottom; the largest feature on the island is a layer of palladium that serves as an additional heat capacity.

into high-impedance coplanar waveguides to serve as capacitors and inductors, respectively. Each microstrip transmission line carrying the signal for a particular polarization and frequency terminates in an impedance-matched 20 Ω resistor on the bolometer island.

The bolometer island is suspended by four silicon nitride legs (Figure 5). The silicon nitride legs carry the antenna transmission and TES bias lines, while also providing a weak thermal link to the bulk of the detector wafer. The bolometer island contains the termination resistor that thermalizes the signal from the antenna, the TES that measures this temperature change, and an additional heat capacity that serves to increase the bolometer thermal time constant. The TESs are held in their superconducting transitions by a tunable bias voltage and operated under negative electrothermal feedback, with a loop gain of ∼5–10.

4.2. Detector Fabrication

The SPT-3G detector wafers were fabricated at the Center for Nanoscale Materials at Argonne National Laboratory. A detailed description of the fabrication process can be found in Posada et al. (2015, 2018); a brief overview is given here.

The detector wafers start as 675 μm thick, 150 mm diameter silicon wafers coated with low-stress silicon nitride. The 300 nm thick Nb ground-plane layer is deposited and patterned to form the sinuous antennas and basic features of the triplexers and bolometers. The wafer is heated to 250°C for the deposition of the 500 nm thick SiO_x dielectric layer to ensure a conformal film. The termination resistors and the TES bolometers are then deposited as thin bimetallic films, consisting either of Ti/Au (Carter et al. 2018) or Al–Mn (Anderson et al. 2020), with similar performance from both types of devices. The top layer of Nb is then deposited and patterned using a two-step process: lift-off for the TES and resistor leads, and etching for the microstrip and array-level wiring. An 850 nm thick layer of palladium is deposited on the bolometer islands and partially overlaps the TES to serve as an additional heat capacity. Lastly, the wafers are diced to their final dimensions, and an XeF_2 etch removes the silicon beneath the bolometer islands.

4.3. Detector Properties

The electrothermal properties of the bolometers define their stability and noise performance. Sources of non-photon noise in the detectors include the Johnson noise in the TES bolometers, thermal fluctuations between the bolometers and the bath (or phonon noise), and noise in the readout system. These noise sources generally increase with detector saturation power, $P_{\rm sat}$, and so control over this parameter is critical for the instrument performance. Our target for $P_{\rm sat}$ is twice the expected optical loading values shown in Table 2; this keeps $P_{\rm sat}$ low while enabling stable operation under a range of observing conditions. Both the TES transition temperature, $T_{\rm c}$, and the thermal conductance to the bath, G, affect $P_{\rm sat}$, as discussed in Ding et al. (2018). To achieve a different $P_{\rm sat}$ for each observing band, $T_{\rm c}$ is held fixed while G is adjusted by altering the bolometer leg lengths. The TES normal resistance, $R_{\rm N}$, is the same for all detectors, as its optimal value is constrained predominantly by the readout; see Section 5 for a discussion of readout noise.

The bolometer thermal time constant, $\tau_{\rm eff}$, is set by G, the heat capacity of the bolometer island, C, and the loop gain of the electrothermal feedback, $\mathcal{L}$, according to the following equation:

$$\tau_{\rm eff} = \frac{C}{G}\frac{1}{1+\mathcal{L}}. \quad (1)$$

For stable TES operation, the thermal response time of the bolometers must be slower than that of the feedback circuit, but a fast thermal time constant is desired to preserve the angular resolution of the instrument along the telescope's scanning direction. These competing requirements restrict $\tau_{\rm eff}$ to lie in the range of ∼1–10 ms. Accurate measurements of $\tau_{\rm eff}$ can be used to deconvolve each detector's temporal response function from time-ordered data before mapmaking for science analyses.

In Table 4, we give the measured values of selected parameters for the deployed detector wafers. Wafers were fabricated in batches of five, with occasional changes to target parameters and layer geometries, based on feedback from laboratory testing, leading to some level of variation between batches. The best performing wafers across batches were then chosen for final installation into the instrument. Eight detector wafers were also characterized on the instrument during the 2018 observing season (Dutcher et al. 2018), while wafers w204 and w206 were installed in 2018 December to replace two wafers with lower performance.

5. Readout

SPT-3G uses a 68× digital frequency-domain multiplexing architecture (Bender et al. 2014, 2016). In this scheme, each bolometer is biased with an AC voltage at a unique frequency between 1.6 and 5.2 MHz, corresponding to the resonant frequencies of a parallel network of LC filters in which the detectors are embedded ($L = 60\,\mu$H, $C = 14$ to 148 pF). Incident radiation from the sky modulates the resistance of each bolometer, and therefore the amplitude of the current flowing through it. Each LC network is composed of lithographed interdigitated capacitors and spiral inductors on silicon chips, which are mounted behind the detector wafers at the same temperature stage (Figure 3).

After a group of 68 multiplexed channels (henceforth referred to as a *multiplexing module*) are summed, the signals

Table 4
SPT-3G Detector Properties

Wafer	R_N (Ω)	T_c (mK)	P_{sat} (pW) 95/150/220	G (pWK^{-1}) 95/150/220	τ_{eff} (ms) 95/150/220	Readout NET ($\mu k\sqrt{s}$) 95/150/220	Total NET ($\mu k\sqrt{s}$) 95/150/220
w172	2.1	423	11/12/12	99/112/112	8/10 /6	202/171/881	516/451/1598
w174	2.2	414	11/14/14	108/151/139	10/10 /8	223/191/1141	551/466/1688
w176	2.2	493	15/17/18	102/120/120	5/5/4	383/316/1385	851/623/1962
w177	2.1	487	13/15/15	100/116/115	4/4/3	258/220/1048	637/487/1673
w180	2.0	460	...	...	7/7/5	201/185/1177	551/480/1811
w181	2.0	469	12/14/14	111/124/122	5/6/3	214/160/926	651/472/1558
w188	2.0	459	11/13/12	90/109/104	9/8 /7	218/187/1080	558/469/1650
w203	2.6	...	...	...	4/5 /2	196/139/828	529/426/1516
w204	2.7	432	11/16/18	103/136/157	4/4/2	242/198/1174	605/482/1738
w206	1.8	444	10/13/15	85/113/128	5/4/2	169/133/949	619/484/1761

Note. Median values of the TES normal resistance, R_N, transition temperature, T_c, bolometer saturation power, P_{sat}, dynamic thermal conductance, G, optically loaded thermal time constant, τ_{eff}, NET from the readout noise per bolometer for each SPT-3G detector wafer, and total NET per bolometer are shown. Parameters are split by observing band, where pertinent, and horizontal lines indicate wafer fabrication batches. Some testing data was not available for all wafers. NET measurements are taken in situ in the deployed instrument, and are described in more detail in Sections 5.1 and 7.5.

are carried on broadside-coupled NbTi striplines to NIST SA13 SQUID series arrays ($L_{input} = 60$ nH to 80 nH), mounted at the 4K stage of the detector cryostat (Stiehl et al. 2011; Doriese et al. 2015; Bender et al. 2018). Since SQUIDs are nonlinear amplifiers with a limited dynamic range, we use a digital active nulling (DAN) feedback scheme to linearize their performance (de Haan et al. 2012). DAN uses an integral feedback loop operated by a field-programmable gate array (FPGA) on room-temperature ICE electronics (Bandura et al. 2016) to null the signals in a narrow band (∼few kilohertz) around each detector bias frequency, removing the vast majority of current at the SQUID input coil due to the bolometer bias. This has the additional benefit of creating a virtual ground before the SQUID input coil, eliminating the impedance of the input coil in series with the bolometer, and therefore improving detector linearity. The sky signal is reconstructed by digitally demodulating this nuller signal in a narrow band around each bias frequency.

The readout electronics are designed to achieve detector stability, low readout noise-equivalent power (NEP), and low crosstalk between detectors. TES bolometers become unstable when the impedance in series with the bolometer is a significant fraction of the detector operating resistance. This requires minimizing the inductance of the wiring between the LC network and the SQUIDs, motivating the use of low-inductance, low thermal-conductivity NbTi striplines, electrically connected using an ultrasonic soldering system described in Avva et al. (2018). In addition, it also defines a minimum operating resistance for the TES bolometers. Achieving a low readout NEP generally pushes the detector resistance in the opposite direction: for a lower-resistance detector, readout current noise terms refer to a smaller power at the detector. At the same time, the SQUID input inductance and the bolometer resistance act as a current divider for the readout noise terms between the SQUID output and integral feedback loop, which imposes a further requirement that the SQUID input impedance be small relative to the bolometer resistance (Bender et al. 2018). Several distinct mechanisms produce electrical crosstalk, which can be mitigated by careful design choices, as described in Section 5.3.

5.1. System Noise

We measure the readout noise in situ by tuning the detectors as usual, then slewing the telescope to the horizon, where the optical power from the atmosphere saturates the bolometers. This eliminates the photon and phonon noise, leaving only the readout noise (dominant) and the TES Johnson noise (subdominant) contributions. The conditions of the measurement modify the observed noise: the lack of detector responsivity no longer suppresses the TES Johnson noise, resulting in an increase to this noise source; and the incident atmospheric power raises bolometer resistances out of the transition to the normal resistance, R_N, slightly decreasing the observed readout noise. Each of these effects modify the measured noise by less than 10%, and oppose one another, so that noise measured at the horizon is a good approximation of the total readout noise in transition. In this configuration, the median measured readout noise is $10.4/13.0/16.0$ pA$/\sqrt{\text{Hz}}$ for 95/150/220 GHz detectors. The correlation of the readout noise with the observing band occurs because the readout noise increases with the detector bias frequency, and the 95 150, and 220 GHz detectors are arranged in consecutive blocks of increasing bias frequency (Montgomery et al. 2021). In Table 4, we compare the readout noise, converted to an effective noise-equivalent temperature (NET), to the total NET from all noise sources. The contribution of the readout to the total NET is largest at 220 GHz, which reflects the higher intrinsic readout noise, lower detector responsivity (Section 7.2), and lower optical efficiency of this band relative to 95 and 150 GHz bands. Total NET values are measured using the median noise with the detectors in transition, which is measured daily across the entire 2019 observing season.

5.2. Detector and Readout Yield

Several stages of characterization during integration and commissioning defined the set of operable detectors. The first of these was a room-temperature continuity check at the wafer, which identified TES channels that were open, shorted to their neighboring detectors, or shorted to ground, primarily due to a combination of wafer fabrication and wirebonding defects. The wirebonds of channels shorted to ground were removed to prevent the entire multiplexing module from being shorted to

ground. In total, 14,166 out of 15,720 detectors (90.1%) tested passed the room-temperature continuity check.

After cooling the receiver to its operating temperature, we performed a network analysis by sweeping a voltage tone across the bandwidth containing LC multiplexer resonances and recording the resulting current through the system, thereby mapping out resonances corresponding to known detectors. We identified valid resonances for 14,261 detectors (90.7%), a higher yield than our warm continuity check because many channel-to-channel shorts at room temperature remain $>1\,\mathrm{k}\Omega$ at cryogenic temperatures. We further pruned the set of operable detectors with additional network analyses performed under a 300 K optical load, above and below the TES critical temperature; the resonance shapes under these conditions can indicate detectors that are insensitive to incident radiative power (e.g., due to defects in the TES fabrication). This was the most significant cut, removing 1718 potential detectors. Additionally, ten full multiplexing modules were disabled because of elevated SQUID or readout noise, or because shorts to ground on the detector array generated thermal heating when operated (660 detectors). After all cuts, we operated a median of 11,424 detectors (72.7%) during the 2019 observing season.

5.3. Crosstalk

Electrical crosstalk between the bolometers in SPT-3G is predominantly sourced within a multiplexing module. There are three expected origins of this crosstalk (Dobbs et al. 2012; Montgomery et al. 2021). First, as described above, the resonant bandwidths of LC filters that are nearest neighbors in frequency have nonzero overlap. This allows a modulation of the resistance of one bolometer to modulate the amplitude of the AC tone biasing the neighbor, producing a crosstalk signal. Second, the wiring impedance in series with the $\mathrm{LCR_{TES}}$ network creates a divider for the applied voltage biases. As the bolometer resistances modulate in response to sky signals, the voltage ratio of this divider is similarly modulated. Last, pairs of planar spiral inductors have a nonzero mutual inductance, which can result in crosstalk.

Dense observations of RCW38 (Section 6.2) are used to measure the crosstalk in SPT-3G. In these data, the telescope is rastered such that every detector in the focal plane sees the source, and individual maps are made for each detector. A template model for RCW38 is used to extract the baseline amplitude for the crosstalk *source* detector and then also at the positions of the other *recipient* detectors within that multiplexing module (Bender et al. 2020). Crosstalk components from source detectors within a $5'$ radius of the recipient RCW38 centroid are excluded to prevent confusion due to the extended source profile. Taking the inverse variance weighted average across 28 observations, we find that 89% of the crosstalk components meet our design target of $<0.5\%$. The slight excess of detector pairs with crosstalk $>0.5\%$ is correlated with channels whose LC resonant frequencies scattered closer to their nearest-frequency neighbor than the design. No crosstalk is detected when the analysis is extended to include recipient detectors in other multiplexing modules, indicating that crosstalk is primarily within a module. Due to the low overall instrument crosstalk, we find no need to analytically remove the measured crosstalk from our data, as we have done for past experiments (Henning et al. 2018). The effect of any residual cross talk is accounted for in the calibration.

5.4. Data Acquisition

The detector data are digitized and sampled at 152.5 Hz, packetized by the FPGAs in the ICE readout electronics, and streamed over gigabit ethernet. These data are serialized and written to disk at a rate of about $20\,\mathrm{MB\,s^{-1}}$ by the DAQ software (part of the `spt3g_software` package SPT-3G Collaboration 2019) running on a computer on the readout network, using the `cereal` library (Grant & Voorhies 2017). The DAQ also mediates the transfer of housekeeping information from the readout electronics and telescope information from the General Control Program (GCP). GCP is an independent process that handles the telescope control and pointing, and is sampled at a lower rate than detector data (Story et al. 2012).

After each observation, detector data are compressed by a factor of $\sim$8 using the lossless FLAC compression algorithm[39] and merged with the housekeeping, calibration, and pointing information to form the raw data that is the input to the data analysis and mapmaking pipeline. The SPT-3G observing cadence results in about 300 GB of compressed data stored to disk daily. To facilitate data transfer from the South Pole for timely data analysis, we further downsample the time-ordered data by a factor of 2 and remove the demodulator quadrature that is out-of-phase with the bolometer response. These downsampled data are transferred every day via the TDRS satellite network, and are primarily used for analyses that do not require high-resolution ($\lesssim 2'$) maps. In addition to the full downsampled data set, about half of the full-rate (compressed) data are also transferred north via TDRS each day; the rest of the full-rate data remain on local storage at the South Pole until they can be shipped out during the austral summer season each year. Some online data processing is performed on the computing system at the South Pole in near real time, such as analysis of calibration data, preliminary mapmaking for monitoring data quality, and a transient alert pipeline.

6. Observing Strategy

6.1. CMB Field Observations

The SPT-3G main survey covers a $1500\,\mathrm{deg^2}$ footprint extending from $20^{\mathrm{h}}40^{\mathrm{m}}0^{\mathrm{s}}$ to $3^{\mathrm{h}}20^{\mathrm{m}}0^{\mathrm{s}}$ R.A., and $-42°$ to $-70°$ decl. Our choice of the survey footprint, shown in Figure 6, is motivated by the need for high-resolution, low-noise CMB maps to remove the *B*-modes induced by gravitational lensing, which contaminate searches for inflationary degree-scale *B*-modes in BICEP/Keck data (BICEP2 Collaboration et al. 2018; BICEP/Keck Collaboration et al. 2021). As a result, the SPT-3G footprint was chosen to closely match that of BICEP Array (Moncelsi et al. 2020). From early December to early March, the Sun produces a detectable signal in the main survey field because of diffraction sidelobes from panel gaps in the primary mirror (George et al. 2012). Starting in the 2019–2020 austral summer, and continuing in the 2020–2021 austral summer, we began a summer-only extended survey that extends to both higher R.A. and higher decl., similar to Bleem et al. (2020; see *SPT-3G extended* in Figure 6). The SPT-3G extended survey will provide a larger sample of galaxy clusters and improved cosmological constraints because of its increased sky fraction.

[39] https://xiph.org/flac

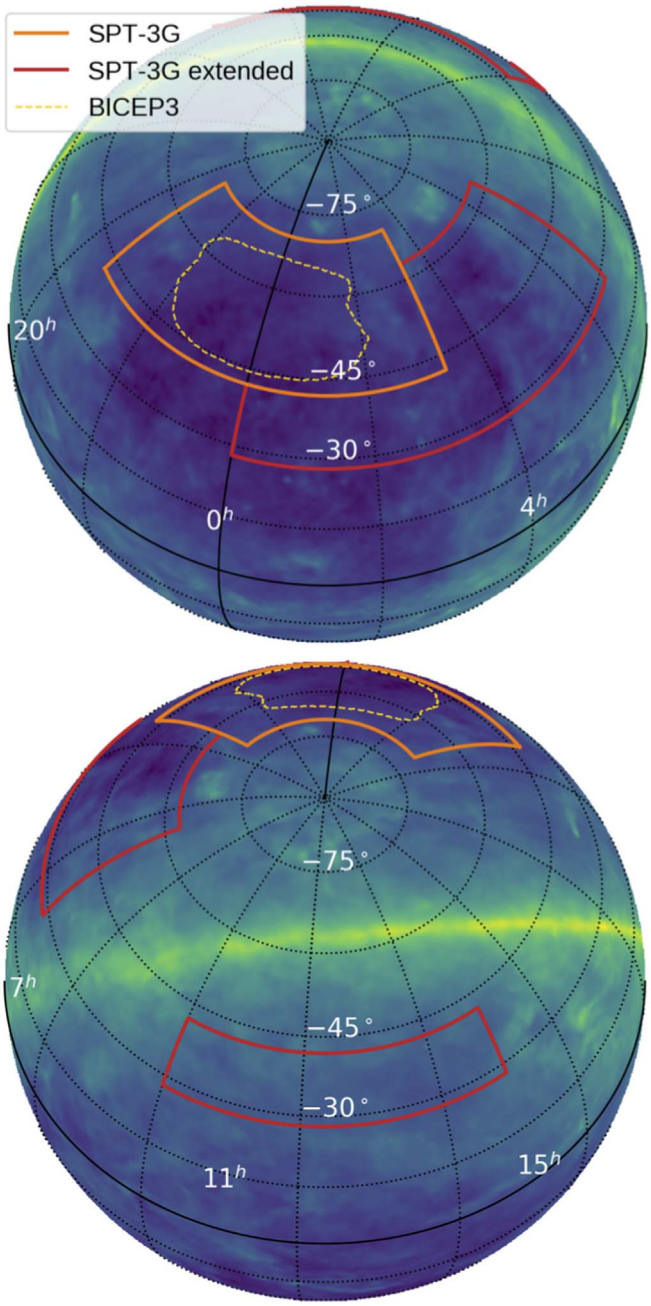

Figure 6. Footprints of the SPT-3G 1500 deg^2 survey (orange solid), the SPT-3G extended survey (red solid), and BICEP3 survey (Ahmed et al. 2014; yellow dotted), overlaid on the Planck thermal dust map (Planck Collaboration et al. 2016a). The BICEP Array (Moncelsi et al. 2020) survey area (not shown) is expected to have a similar footprint to BICEP3. The yellow contour is chosen to correspond to an effective sky fraction at the mean survey weight. Since BICEP3 has a much larger field of view than SPT-3G, there is significant sky area outside the yellow contour, but still overlapping with the SPT-3G survey, on which BICEP3 has nontrivial survey weight.

The main survey footprint is divided into four subfields centered at −44.75°, −52.25°, −59.75°, and −67.25° decl., respectively, to limit the variation in detector responsivity throughout each observation. Similar to previous SPT surveys (e.g., Henning et al. 2018), we observe the CMB by rastering the telescope across a subfield at a constant elevation, taking a 12.′5 step in elevation, then repeating until the full elevation range of the subfield has been observed, taking a total of ∼2 hr. The raster scans composing each subfield observation have a small global elevation offset of $N \times 0.'5$, with $0 \leqslant N < 25$, known as *dither steps*, improving the uniformity of coverage in coadded maps.

6.2. Calibration Observations and Relative-calibration Procedure

In addition to observations of each CMB subfield, a suite of calibration observations is regularly performed to convert the time-ordered data into units of CMB blackbody temperature. This conversion depends on the optical-power incident on each detector, which varies due to changes in weather and the fact that SPT-3G observes the regions of sky spanning elevations from 28° to 70°. While the final temperature calibration of SPT maps is performed by cross-correlating with Planck maps (Section 7.4), this initial time-domain calibration is used to weight and coadd individual observation maps.

The first step in the calibration chain entails a dense raster scan of one of the Galactic H II regions, RCW38 or MAT5a (NGC 3576; Coble et al. 2003), in which every detector scans over the source (henceforth referred to as a *dense observation*). Both H II regions are observed in this manner every eight days. RCW38 is used for the calibration of the two lower-elevation subfields of the 1500 deg^2 survey, while MAT5a is used for the two higher-elevation fields. The H II regions have known reference flux from previous Planck-calibrated observations by SPT-SZ (Mocanu et al. 2019). A map for each bolometer in a dense observation is fit to a band-averaged template, and the fitted source flux is compared to the reference flux to obtain the calibration of each detector in CMB temperature units. Since the dense observations are taken infrequently, two corrections must be applied to obtain accurate relative temperature calibrations for each CMB field observation.

First, a detector's responsivity may be different during a CMB observation than during the most recent dense observation, due to changes in optical-power incident on the detector or detector voltage bias. A chopped thermal source is located behind a small aperture in the secondary mirror and illuminates all detectors in the focal plane. The response to this source is measured both immediately before the dense observation, as well as before every CMB field observation, and the ratio of these two responses is used to correct for changes in the detector responsivity.

A second correction accounts for changes in atmospheric transmission between the time of the dense observation and a CMB field observation. Immediately before every CMB field observation, we perform a faster, sparse raster scan of one of the H II regions, in which only a subset of detectors scans over the source (henceforth referred to as a *sparse observation*), and we also measure the response of the detectors to the chopped thermal source. The time-ordered data for the sparse observation are calibrated in units of watts at the TES and corrected for the difference in detector responsivity between the sparse and dense observations as described in the previous paragraph. For each band, we form a coadded map of these time-ordered data from the sparse observation, and another coadded map from the most recent dense observation of the same H II region. The band-averaged atmospheric transmission T_ν, at the time of the sparse observation $t_{\rm sparse}$, relative to the dense observation at $t_{\rm dense}$, in each observing band ($\nu \in \{95, 150, 220\,{\rm GHz}\}$), is then

defined as the ratio of integrals of the maps over a $4' \times 4'$ box:

$$T_\nu(t_{\rm sparse}) \equiv \frac{\int_{4'\times4'} M_\nu(\Omega;\, t_{\rm sparse})\, d\Omega}{\int_{4'\times4'} M_\nu(\Omega;\, t_{\rm dense})\, d\Omega}, \quad (2)$$

where M_ν is the coadded map of the sparse or dense observation of the H II region. Note that coadded maps are constructed from a subset of bolometers in the focal plane that observe the chopped source and H II region with high signal-to-noise.

Taking these effects together, C_i, the conversion from electrical power at the TES to CMB temperature for bolometer i, is expressed as

$$C_i(t_{\rm CMB})[\mathrm{W\ K^{-1}}] = \frac{R_i(t_{\rm CMB})[\mathrm{W}]}{R_i(t_{\rm dense})[\mathrm{W}]} \times T_{\nu(i)}(t_{\rm sparse}) \times \frac{\hat{A}_i \int_{4'\times4'} M_{\nu(i)}(\Omega;\, t_{\rm dense})[\mathrm{W}]\, d\Omega}{\int_{4'\times4'} M^{\rm ref}_{\nu(i)}(\Omega)[\mathrm{K}]\, d\Omega}, \quad (3)$$

where $R_i(t)[\mathrm{W}]$ is the response of bolometer i to the chopped thermal source at time t in units of watts at the TES, with $t_{\rm CMB}$ and $t_{\rm dense}$ being the times of a CMB observation and its preceding dense H II region observation, respectively; $M^{\rm ref}_{\nu(i)}(\Omega)[\mathrm{K}]$ is the reference map from SPT-SZ of the H II source calibrated in units of $\mathrm{K_{CMB}}$; and $\hat{A}_i$ is a best-fit amplitude parameter obtained by a linear least-squares fit of a dense H II region map for bolometer i to a template $M_{\nu(i)}(\Omega; t_{\rm dense})$ constructed from a map coadded across a set of detectors. Coadded maps created using this calibration have an absolute calibration that is within 10% of that of Planck, with nonidealities caused by differences in the bandpasses and beams between SPT-3G and SPT-SZ.

7. Integrated Performance

7.1. Detector and Readout Yield

Several stages of characterization during integration and commissioning defined the set of operable detectors. The first of these was a room-temperature continuity check at the wafer, which identified TES channels that were open, shorted to their neighboring detectors, or shorted to ground, primarily due to a combination of wafer fabrication and wirebonding defects. The wirebonds of channels shorted to ground were removed to prevent the entire multiplexing module from being shorted to ground. In total, 14,166 out of 15,720 detectors (90.1%) tested passed the room-temperature continuity check.

After cooling the receiver to its operating temperature, we performed a network analysis by sweeping a voltage tone across the bandwidth containing LC multiplexer resonances and recording the resulting current through the system, thereby mapping out resonances corresponding to known detectors. We identified valid resonances for 14,261 detectors (90.7%), a higher yield than our warm continuity check because many channel-to-channel shorts at room temperature remain $>1\,\mathrm{k\Omega}$ at cryogenic temperatures. We further pruned the set of operable detectors with additional network analyses performed under a 300 K optical load, above and below the TES critical temperature; the resonance shapes under these conditions can indicate detectors that are insensitive to incident radiative power (e.g., due to defects in the TES fabrication). This was the most significant cut, removing 1718 potential detectors. Additionally, ten full multiplexing modules were disabled because of an elevated SQUID or readout noise, or because shorts to ground on the detector array generated thermal heating when operated (660 detectors). After all cuts, we operated a median of 11,424 detectors (72.7%) during the 2019 observing season.

7.2. Optical Efficiency

The overall sensitivity of the experiment is dependent on the cumulative optical efficiency of the instrument, which we characterize using the same single-detector maps of RCW38 described in Sections 5.3 and 6.2. These single-detector maps are compared against the known brightness temperatures of RCW38 in each band, yielding a cumulative optical efficiency measurement, η, for every detector.

To calculate η, the integrated flux across the source is measured by each detector in units of W·sr, using the voltage and current calibrations from the readout electronics. Coadded maps of RCW38 in units of $\mathrm{K_{CMB}}$, which are absolutely calibrated against Planck (Mocanu et al. 2019), are then used to infer the integrated flux that would be measured by a perfectly efficient polarization-sensitive detector and receiver with top-hat spectral response and with band centers and widths as defined in Section 7.3. The ratio of these two quantities provides a measurement of η.

This measurement is limited by any systematic errors in accurately converting between a change in measured current at the TES and a change in the optical power deposited at the TES. These power calibration errors are largely due to small fluctuations in the parasitic impedances in the readout circuit, which are a complicated function of bias frequency and not very well constrained. Specifically, we define $\eta_{\rm fmux}$ as the quantity obtained from the procedure described above, which we claim is related to $\eta_{\rm true}$ through

$$\eta_{\rm fmux} = \frac{1}{2} V_{\rm fmux} \frac{dI_{\rm fmux}}{dI_{\rm true}} \frac{dI_{\rm true}}{dP_{\rm true}} \eta_{\rm true}, \quad (4)$$

where $V_{\rm fmux}$ is the measured voltage bias across the TES, the first derivative term describes the readout system's transfer function when measuring current across the TES, and the second derivative term is the true responsivity of the detector under an AC bias (Irwin & Hilton 2005).

In the limit of high loop gain, low parasitic resistances, and a negligible readout system transfer function, we have $\eta_{\rm fmux} \approx \eta_{\rm true}$. However, the SPT-3G readout system has nonnegligible parasitic series impedances at lower bias frequencies. These parasitics generate a slight current bias, boosting the responsivity of the 95 and 150 GHz detectors. The 220 GHz detectors are operated at higher bias frequencies, where this series impedance is smaller (Montgomery 2021). They, therefore, have a lower total responsivity, but also provide a means for roughly normalizing the excess responsivity of the 95 and 150 GHz detectors.

Although it is challenging to accurately estimate the magnitude of these systematic effects from our incomplete knowledge of the circuit dynamics, we have attempted to remove them using their correlation with the readout system bias frequencies. In other words, we argue that $\eta_{\rm true}$ should be uncorrelated with bias frequency, apart from the two

Table 5
Measured SPT-3G Optical Efficiency, η

Wafer	95 GHz	150 GHz	220 GHz
w172	0.21 ± 0.04	0.35 ± 0.10	0.11 ± 0.02
w174	0.24 ± 0.04	0.37 ± 0.07	0.11 ± 0.04
w176	0.21 ± 0.03	0.36 ± 0.06	0.13 ± 0.03
w177	0.23 ± 0.03	0.39 ± 0.05	0.14 ± 0.02
w180	0.29 ± 0.05	0.46 ± 0.07	0.12 ± 0.03
w181	0.24 ± 0.05	0.49 ± 0.12	0.16 ± 0.04
w188	0.29 ± 0.04	0.48 ± 0.12	0.14 ± 0.03
w203	0.25 ± 0.04	0.49 ± 0.10	0.14 ± 0.04
w204	0.31 ± 0.08	0.50 ± 0.10	0.13 ± 0.03
w206	0.32 ± 0.09	0.59 ± 0.25	0.17 ± 0.05
Full Array	0.25 ± 0.07	0.44 ± 0.14	0.13 ± 0.04
Predicted	0.27	0.38	0.22

Note. 13 calibration observations during the 2019 austral winter were used to determine the median η of every operating detector. These values were used to determine the medians and standard deviations across each wafer, as well as across the full array. The predicted efficiencies are based on the model presented in Table 2.

discontinuities associated with observing band changes (detector bias frequencies are grouped by observing band, which we do expect to have different values of $\eta_{\rm true}$). For every wafer, we fit a function encapsulating the bias-frequency dependence of $\eta_{\rm fmux}$ and remove it, thereby removing all systematic readout calibration and responsivity effects dependent on bias frequency, up to a single overall scaling factor for all three bands. In light of the fact that the 220 GHz detectors are the least affected by this systematic, this overall scaling factor is constrained so that the median 220 GHz η value for each wafer is preserved pre- and post-correction. On average, this correction process results in a 29% and 15% downward shift in the estimated cumulative efficiencies for the 95 and 150 GHz channels, respectively.

In Table 5, we report the median η measurement for each wafer and the full array. The variation of median values between wafers is likely dominated by the uncertainty associated with the median $\eta_{\rm fmux}$ 220 GHz value, to which each wafer's corrected η is scaled. Considering the full array, the 95 and 150 GHz efficiencies agree with predicted efficiencies based on the optical model and known element properties of the instrument, whereas the 220 GHz channels underperform predictions.

The consistency of measured and predicted optical loading in Section 3 suggests that the level of unaccounted scattering or reflection through the system should not be unexpectedly high. Our current conclusion is that our laboratory measurements of dielectric loss through alumina underestimated the 220 GHz signal attenuation through our multiple alumina elements, and that the details of the manufacturing process affected the optical properties of the final elements. It is plausible that the optical properties of the larger monolithic elements may differ from those of the smaller samples explored during laboratory testing, despite nominally being the same formulation from the same vendor.

7.3. Spectral Response

The SPT-3G receiver spectral response, averaged across the detector array and for each detector wafer, is shown in Figure 7.

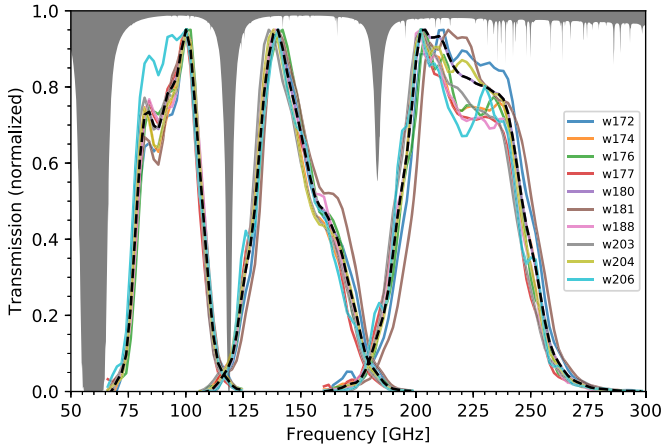

Figure 7. Frequency response, $g(\nu)$, of the SPT-3G receiver at 95, 150, and 220 GHz to a beam-filling, flat-spectrum source. The solid lines show the response averaged by detector wafer, and the dashed line is the average response across all ten wafers. The gray shaded region indicates atmospheric absorption for 0.25 mm precipitable water vapor at the South Pole. The frequency response has been arbitrarily normalized. The power on the detector, P, for a source with a spectrum, $I(\nu)$, would be $P = \int \eta_g\, g(\nu) I(\nu) d\nu$, where η_g is the optical efficiency.

Table 6
Measured Array-averaged Instrument Parameters

	95 GHz	150 GHz	220 GHz
Measured Optical Efficiency	0.25 ± 0.07	0.44 ± 0.14	0.13 ± 0.04
(excluding stop efficiency)	0.45	0.54	0.14
Band Center (GHz)	93.8 ± 0.7	147.0 ± 1.2	219.9 ± 2.0
Band Width (GHz)	26.4 ± 1.2	32.5 ± 0.7	53.6 ± 1.9
Beam FWHM (arcminutes)	1.57	1.17	1.04
Median NET (μk$\sqrt{\rm s}$)	9	8	28
T Map Depth (2019+2020), $3000 < \ell < 5000$ (μK-arcmin)	5	4	15
Polarization-angle Uncertainty (deg)	2.0	2.2	4.5

Note. In addition to the measured instrument optical efficiency taken from Section 7.2, we quote the same efficiency measurement after excluding the predicted Lyot stop spillover loss, as described in Table 2. The band center is defined as $\int \nu g(\nu) d\nu / \int g(\nu) d\nu$ and bandwidth defined as $\int g(\nu) d\nu$, where $g(\nu)$ is the SPT-3G receiver frequency response (normalized to 1) to a beam-filling, flat-spectrum source (as shown in Section 7.3). The uncertainties reflect the spread across detector wafers.

The array-averaged band center and width are summarized in Table 6. The spectral response was measured in situ with a compact Fourier transform spectrometer, described in Pan et al. (2018, 2019). The measurement gives the SPT-3G receiver response to a beam-filling, flat-spectrum source at the receiver's vacuum window. Therefore, the shape of the response is due to the combined transmission of the on-wafer triplexer filter, and the optical elements internal to the receiver, including any AR coatings.

7.4. Beams and Absolute Temperature Calibration

The SPT-3G point-source response (the *beam* response) is estimated in a hybrid manner similar to the SPT-SZ beam response (Keisler et al. 2011) using a combination of point sources in the CMB observations and dedicated raster scans of Saturn. These raster observations produce a high signal-to-noise ratio (S/N) measurement of the beam response out to

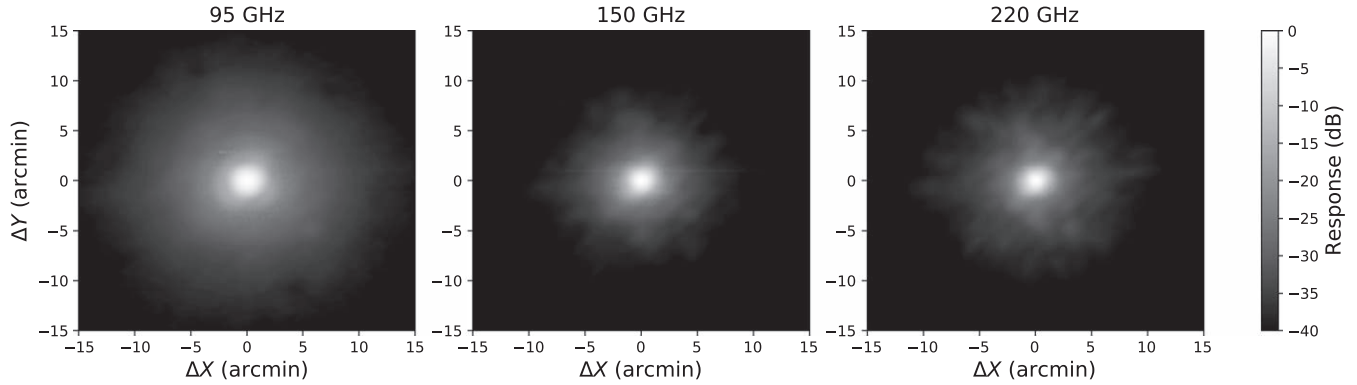

Figure 8. Composite beam response by band formed by stitching together point sources in the science observations with deep raster scans over the planets.

radii of tens of arcminutes; however, the detectors show evidence of nonlinearity and saturation in the form of a suppressed response directly on the planet and a slow decay on the falling edge. The response to point sources in the survey data is significantly more linear; however, the available S/N is insufficient to resolve the extended beam structure. The composite beam shape is calculated by stitching together the planet maps and point sources using a radial range where (a) the beam is resolved at high signal-to-noise in the point-source maps, (b) and the Saturn data can be cleaned of detector saturation.

The Saturn beam response is cleaned of saturation contamination by masking the data within a scan after the detector has come within one beam radius of the planet center until the end of the scan. This method allows each detector to measure the rising edge of the beam and recover from the saturation before approaching Saturn from the other side. This saturation masking radius is set by the extent of artifacts in the difference between the planet maps and the point-source maps. The CMB temperature anisotropies are resolved at a high S/N in our planet raster scans. We subtract the scanned Planck PR3 maps[40] from our planet maps, resulting in a percent-level change in our beam measurement at the largest angular scales. These cleaned planet maps are fit to the field sources and blended to form a composite beam response, shown in Figure 8. After dividing out the small contribution to the beam maps from statistical error in the pointing reconstruction and the finite Saturn disk size, the main lobe of the full detector array effective beam response can be approximated as a Gaussian with an FWHM of $1\farcm57/1\farcm17/1\farcm04$ at 95/150/220 GHz (Table 6).

We perform the same beam calibration using four subsets of the field sources, split by the subfields defined in Section 6.1, using only one of the two deep planet raster scans, and sampling from the covariance of the amplitude and offset parameters used to align the field source and planet maps. We find a statistical uncertainty on our B_ℓ measurement, shown in Figure 9, across the ℓ range of the SPT-3G science results.

We also measure the beam response in cross correlation with the Planck PR3 maps by comparing the temperature auto spectrum of our data with the cross spectrum of our data and the nearest-frequency Planck map. This analysis, described with further detail in Dutcher et al. (2021), provides a method for setting the absolute temperature calibration of SPT-3G coadded maps in each observing band. In addition, this analysis

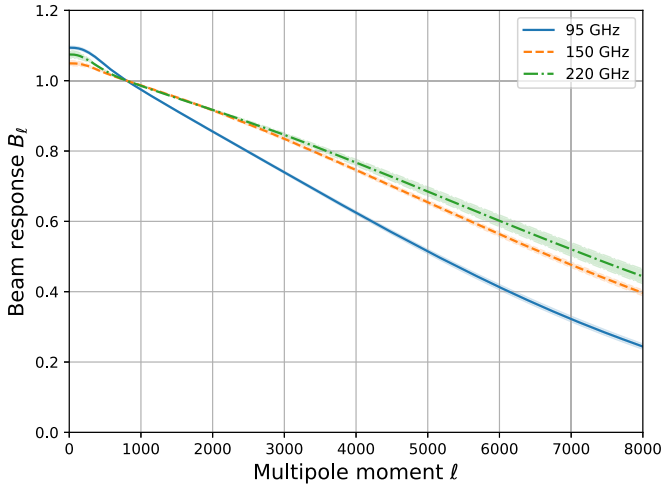

Figure 9. Composite beam response as a function of multipole moment ℓ. The shaded area shows the diagonal of the beam covariance calculated by repeating the computation with different subsets of planet and field source inputs and sampling from the covariance of the stitching parameters. All beam response curves are normalized to unity at $\ell = 800$.

allows us to estimate the beam window function B_ℓ in harmonic space, independent of the main position-space analysis. The harmonic space beam measurement is limited above $\ell \gtrsim 1500$ due to the Planck noise and beam size and below $\ell \lesssim 100$ by the timestream filtering used primarily to reduce atmospheric noise. The uncertainties in this harmonic space beam calibration are established by direct Monte Carlo simulation. We find consistent results with the measured position-space beam analysis over the range of multipoles where the temperature cross spectrum is informative.

7.5. Sensitivity

Over the entire 2019 and 2020 winter observing seasons (2019 March 21 to December 18, and 2020 March 21 to November 26), the fraction of time spent observing the CMB was 58.4%,[41] illustrated in Figure 10. Unscheduled maintenance on the telescope drive system during 2019 June and several brief power outages account for most of the deviation from the optimal 60% efficiency. The primary routine losses of observing time are due to cycling the ^{3}He–^{3}He–^{4}He sorption

[40] https://pla.esac.esa.int/

[41] An additional 3.3% of time spent observing the CMB is removed because the telescope is changing direction in azimuth between consecutive scans and is not moving at constant angular velocity.

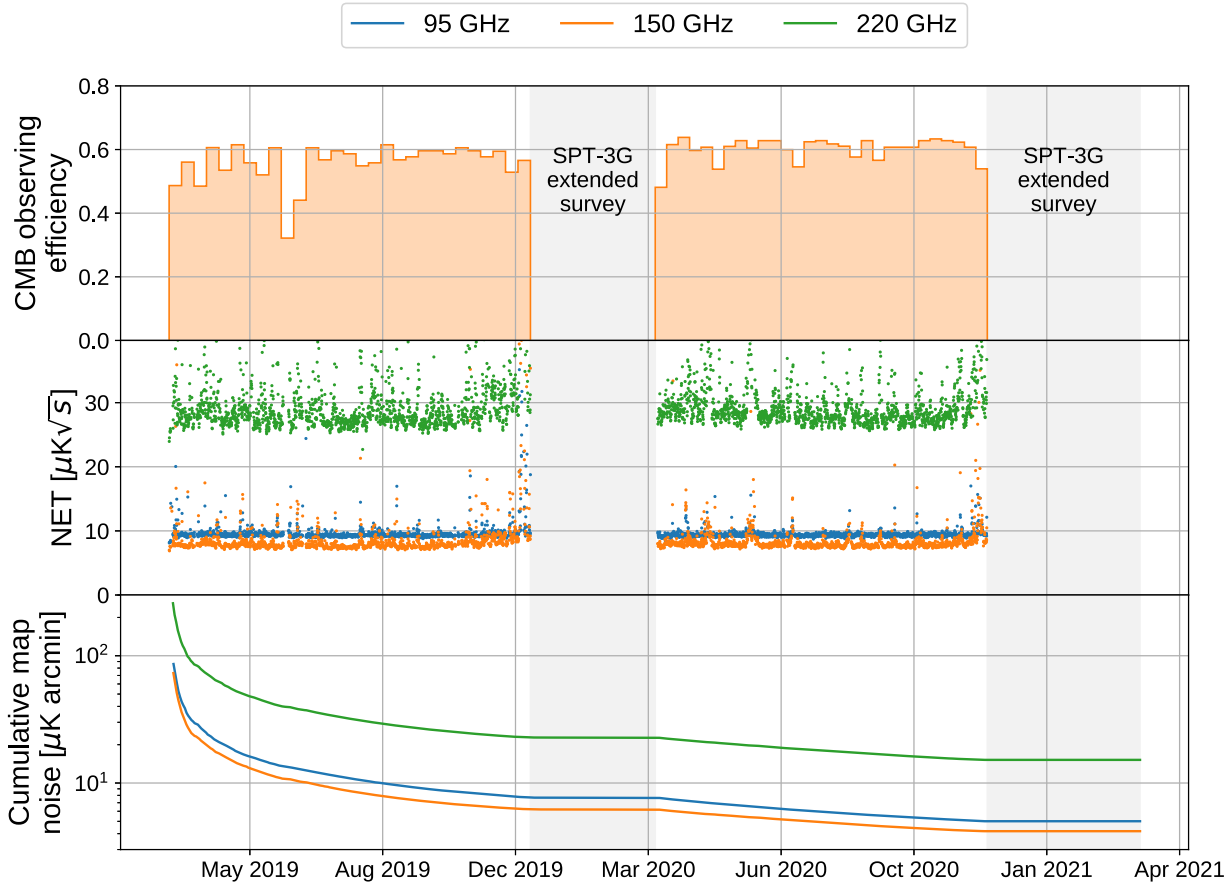

Figure 10. CMB observing efficiency, NET, and integrated noise of the 2019 and 2020 data from SPT-3G. Top: fraction of total calendar time during which SPT-3G observed its main CMB fields. Time not spent observing the CMB was primarily spent tuning detectors, performing calibration observations, and cycling the sorption refrigerator. Middle: array NET inferred from maps of subfield observations in the multipole range $\ell \in [3000, 5000]$ for the 95 GHz (blue), 150 GHz (orange), and 220 GHz (green) detectors. Bottom: depth in temperature of cumulative maps as a function of time. Noise is estimated from angular multipoles of $\ell \in [3000, 5000]$, averaged over the four subfields comprising the SPT-3G main survey. The three curves correspond to the noise of the 95 GHz (blue), 150 GHz (orange), and 220 GHz (green) maps.

refrigerator and retuning detectors (together, 24% loss) and calibration observations (12% loss).

The median NET for the array during the 2019 and 2020 observing seasons was $9/8/28$ $\mu\mathrm{K}\sqrt{\mathrm{s}}$ at $95/150/220$ GHz, and the NETs per observation are shown in Figure 10. To estimate these values, for each observation, we make a map with filtering settings optimized for detection of point sources and galaxy clusters, including a high-pass filter with a cutoff of $\ell = 500$. We then measure the autospectrum of the resulting map in the interval $\ell \in [3000, 5000]$, well above the $1/\ell$ knee of the data. The autospectrum includes both noise and sky signal, but at these multipoles, the sky signal in a single observation is negligible compared with the noise. This map noise is converted to NET using the area of the uniform-coverage portion of the field and the time spent observing it. These maps are created daily, primarily for data-quality monitoring purposes; as such, they do not correct for the filter transfer function, biasing our reported NET to lower values by an ℓ-dependent factor of 5%–10% in the range of $\ell \in [3000, 5000]$. In addition, the temperature calibration for these maps is derived from the H II regions RCW38 and MAT5a, as described in Section 6.2, which results in an additional $\lesssim$10% difference relative to calibrating in cross correlation with Planck. With these caveats, the coadd of these per-observation maps from the 2019 and 2020 winter seasons has a noise level of $5/4/15$ μK arcmin at $95/150/220$ GHz in temperature (Table 6). We plan to continue observing the same sky area with SPT-3G for the next three austral winters (through the end of 2023). Since no major changes to the instrumental configuration or observing strategy are planned, each of these upcoming seasons should have a sensitivity comparable to the level achieved during 2019 and 2020.

At frequencies below 1 Hz, atmospheric temperature fluctuations result in a significant increase in noise above the white photon-noise floor. Since the atmospheric signal is largely unpolarized, these fluctuations can be efficiently removed by differencing timestreams from detectors with orthogonal polarizations in the same pixel. Figure 11 shows the reduction in the low-frequency atmospheric noise achieved by differencing polarization pairs, with spectra measured with the telescope stationary and detectors operating as in CMB observations. Quantitative characterization of the low-frequency noise in the map domain is an area of ongoing study and will be described in future publications that use these data products, while the low-frequency noise performance of the readout electronics is discussed in Bender et al. (2020). In situ measurements of detector-level NETs across the array are shown in the bottom panel of Figure 11. Using our understanding of the SPT-3G optical model, detector properties, and readout system design, we are able to roughly predict (with some caveats) expected detector-level NETs. In comparing these values, we find an acceptable agreement between our

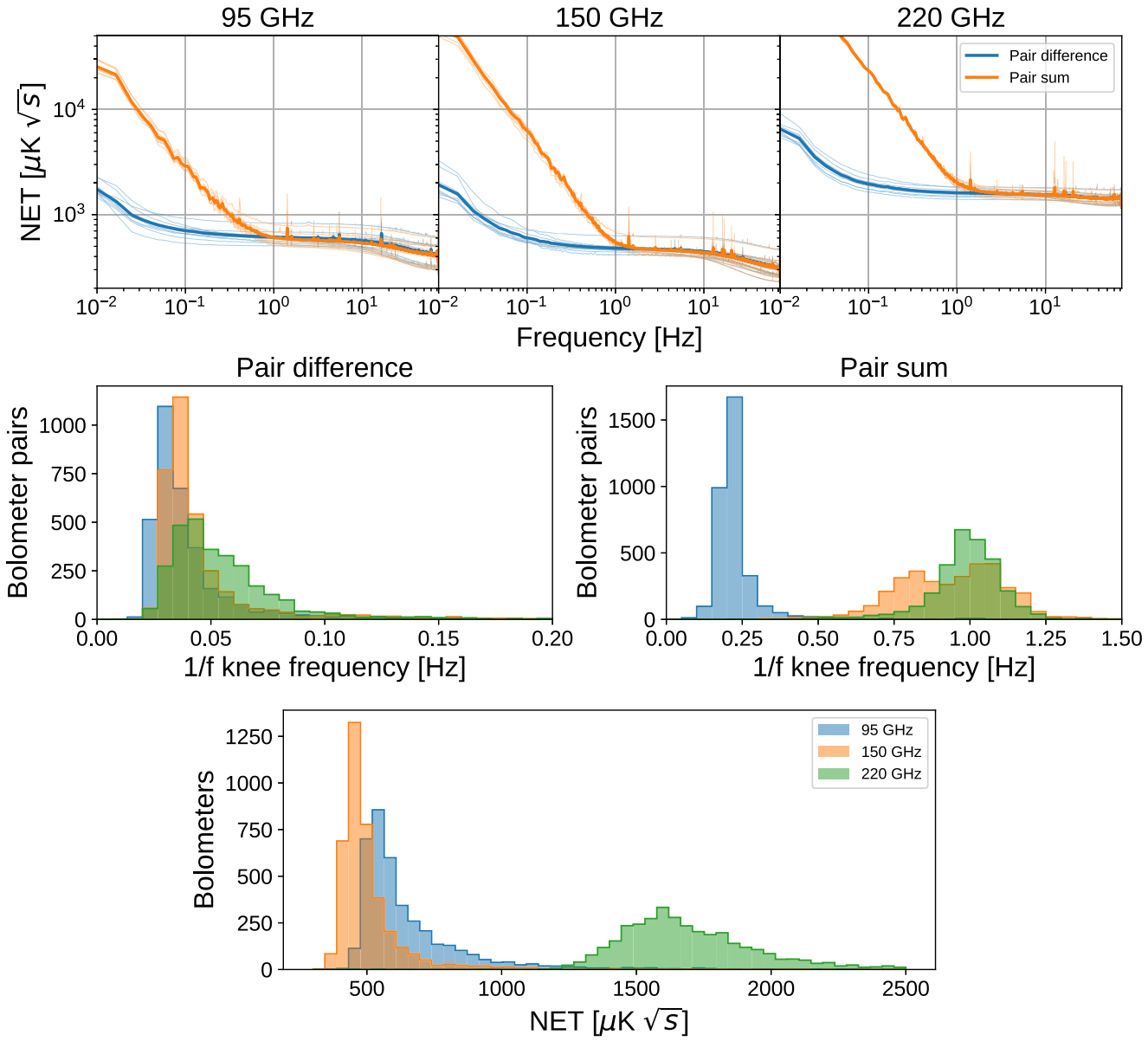

Figure 11. Top panel: mean noise amplitude spectral density for polarization pair sum (orange) and difference (blue) for 95 (left), 150 (middle), and 220 GHz (right) bolometers for the best 90% of noise measurements taken during the 2019 season. Noise observations are taken with the telescope at rest and detectors operating as in CMB observations. Thin lines are averages for individual wafers, while thick lines include all detectors. Middle panel: median $1/f$ knees for the pair difference (left) and pair sum (right) noise spectra from noise observations. Each entry in the histogram corresponds to the knee for a single polarization pair, with the median taken over all noise measurements in 2019. Bottom panel: median NET for all bolometers. Each entry in the histogram corresponds to the noise level for a single bolometer, evaluated between 3 and 5 Hz, with the median taken over all noise measurements in 2019.

measurements and the noise model at 95 and 150 GHz, but elevated noise levels among the 220 GHz detectors. The higher-than-expected 220 GHz NET levels are very likely caused by the instrument's lower-than-expected cumulative optical efficiency across the 220 GHz band (Section 7.2), as well as by the elevated readout system noise at the higher bias frequencies (Section 5.1).

7.6. Polarization Calibration

As described in Section 4.1, each detector wafer contains dual-polarization pixels with an alternating 45° rotation to measure the Q and U Stokes parameters. Given the hexagonal shape of the wafers, each containing detectors with four polarization orientations, there are a total of 12 polarization orientations over the entire detector array, each separated by 15°. Each detector is attributed a nominal polarization angle based on the wafer's orientation during installation. The goal of our polarization calibration procedure is to confirm that each detector has been assigned the correct nominal polarization angle,[42] which we then assume to be its true polarization angle when constructing CMB maps. This assumption results in a modest loss of polarization efficiency, which can likely be improved by further assigning average polarization angles to subsets of detectors that have a systematic polarization rotation

[42] This mapping is not known unambiguously a priori for every detector because of frequency scatter and imperfect yield in the LCR resonators that comprise the multiplexing readout circuit.

relative to the nominal angle (e.g., pixels with left- and right-handed sinuous antennas).

Because of the difficulty in performing polarization calibration with a terrestrial source in the far-field of a large-aperture CMB telescope, we use dedicated observations of Centaurus A (CenA, NGC 5128) to derive the relative polarization angles of detectors by fitting its large, arcminute-scale, polarized radio lobes. The CenA method is described here and is currently being studied using SPT-3G data. Final results and further discussion of this method, as well as of a similar method using the polarization of the CMB itself, will be included in a future paper.

Each CenA observation takes ∼3 hr and consists of a dense, $0.25'$ raster over a $3^\circ \times 3^\circ$ area, centered on CenA. After the observation, a full-array, polarized coadded map is constructed for each observing band, along with single-detector maps for each detector in the array. Each single-detector map, with observing band b, is then fit to a model template given by

$$t_b = g[(2 - \rho)T_b + \rho\cos(2\Theta)Q_b + \rho\sin(2\Theta)U_b], \quad (5)$$

where T_b, Q_b, and U_b are the observed, per-band detector-array coadded maps; an overall gain (g), polarization angle (Θ), and polarization efficiency (ρ) per detector are the free parameters of the fit. Because the template coadd maps are constructed using the nominal polarization angles, efficiencies, and detector gains, we lose the ability to constrain the absolute global parameters. The fit parameters for each detector are estimated from a least-squares fit of each single-bolometer map to the model template of Equation (5). Since a single observation of CenA by a single bolometer does not provide enough sensitivity to yield a meaningful measurement of its polarization angle, this calibration was performed on a cadence of approximately once per week during the 2019 austral winter.

The polarization angle for each detector was computed for each of 30 observations of CenA during the 2019 season. The mean polarization-angle and associated uncertainty for each detector was estimated by the sample mean and standard error over the 30 calibration observations. With this method, we measure every detector's polarization angle with a median uncertainty of $2.0^\circ/2.2^\circ/4.5^\circ$ for the 95/150/220 GHz detectors (Table 6). This uncertainty is well below the 15° difference between the nominal polarization angles, allowing us to assign each detector to its nominal angle with high confidence. These nominal polarization angles were assumed in the construction of maps for recent analyses of SPT-3G data (e.g., Dutcher et al. 2021), as detailed characterization of any real deviations from these nominal angles is a topic of ongoing study. While these measurements of individual detector polarization angles do not imply significant deviation from nominal angles, it may be possible to correct for deviations from nominal angles by averaging many detectors across the array or a wafer.

At the level of sensitivity expected for SPT-3G, the primary impact of assuming nominal polarization angles during mapmaking is a small decrease in the average polarization efficiency of the experiment. One notable cause of this decrease is the polarization wobble of the sinuous antenna—which we detect at high significance in our analysis of CenA observations —together with our choice to use an equal number of pixels with left-handed and right-handed antennas (Section 4.1). Left-handed and right-handed pixels have polarization angles that are slightly offset by equal and opposite magnitudes from the nominal angle, resulting in a decreased overall polarization efficiency. In Dutcher et al. (2021), we corrected for the change in polarization calibration by comparing the *TE* and *EE* power spectra of SPT-3G to those of Planck, implying polarization efficiencies of 97.2%/94.6%/88.0% for 95/150/220 GHz maps. This comparison indicates that, even without correcting for the mean polarization rotation due to the polarization wobble, the assumption of nominal angles has at most a modest effect on the overall polarization sensitivity. We anticipate an even smaller efficiency loss in maps constructed using the mean measured polarization angles for left-handed and right-handed detectors at each orientation.

8. Conclusion

We have presented the design and integrated performance of the SPT-3G instrument, which has already achieved a temperature map-depth of 5/4/15 μK arcmin at 95/150/220 GHz, using two years of data from a multiyear survey. SPT-3G is currently observing and plans to continue doing so through the end of the 2023 season, providing deep, arcminute-scale resolution CMB maps that will be useful for a wide range of scientific analyses.

Already, measurements of the *EE* and *TE* power spectra using four months of SPT-3G data in 2018 (half of a typical observing season) have improved upon previous results from SPTpol at multipoles $\ell \lesssim 1500$ (Bender et al. 2020), and provided stronger constraints on extensions to the ΛCDM cosmological model (Balkenhol et al. 2021). The instrument's increased detector count has improved the instantaneous sensitivity to small angular-scale features, allowing for near real-time detection of Galactic and extragalactic millimeter-wave transient sources (Guns et al. 2021). Similarly, SPT-3G's large observing footprint and high re-observation cadence provide a powerful look into high-resolution time-domain astrophysics of a large range of sources from blazars to low-luminosity active galactic nuclei and flaring stars.

In addition, analyses are underway to use current data to measure temperature, polarization, and lensing power spectra on arcminute scales to further explore tensions with the ΛCDM model and constrain possible extensions. Joint efforts using SPT-3G data along with BICEP/Keck data to de-lens the *B*-mode polarization power spectrum will provide unprecedented constraints on the energy scale of inflation. SPT-3G maps are also currently being used to expand catalogs of emissive point sources and high-redshift galaxy clusters. The complete SPT-3G survey will produce maps with an unprecedented combination of sensitivity and resolution that will enable significant advances in millimeter-wave astronomy and cosmological constraints from the CMB.

The South Pole Telescope program is supported by the National Science Foundation (NSF) through grants PLR-1248097 and OPP-1852617. Partial support is also provided by the NSF Physics Frontier Center grant PHY-1125897 to the Kavli Institute of Cosmological Physics at the University of Chicago and the Kavli Foundation. Argonne National Laboratory's work was supported by the U.S. Department of Energy, Office of High Energy Physics, under contract DE-AC02-06CH11357. This work was performed, in part, at the Center for Nanoscale Materials, a U.S. Department of Energy Office of Science User Facility, and supported by the U.S. Department of

Energy, Office of Science, under Contract No. DE-AC02-06CH11357. We acknowledge R. Divan, L. Stan, C.S. Miller, and V. Kutepova for supporting our work in the Argonne Center for Nanoscale Materials. Work at Fermi National Accelerator Laboratory, a DOE-OS, HEP User Facility managed by the Fermi Research Alliance, LLC, was supported under Contract No. DE-AC02-07CH11359. N.W.H. acknowledges support from NSF CAREER grant AST-0956135. The McGill authors acknowledge funding from the Natural Sciences and Engineering Research Council of Canada, Canadian Institute for Advanced Research, and the Fonds de recherche du Québec Nature et technologies. This material is based upon work supported by the U.S. Department of Energy, Office of Science, Office of High Energy Physics under Award Number DE-SC-0015640. M.A. and J.V. acknowledge support from the Center for AstroPhysical Surveys at the National Center for Supercomputing Applications in Urbana, IL. J.V. acknowledges support from the Sloan Foundation.

Facility: Amundsen–Scott South Pole Station.

Software: IPython (Perez & Granger 2007), LMFIT (Newville et al. 2014), Matplotlib (Hunter 2007), NumPy (van der Walt et al. 2011), Pandas (McKinney 2010), and SciPy (Jones et al. 2001).

ORCID iDs

J. A. Sobrin https://orcid.org/0000-0001-6155-5315
A. J. Anderson https://orcid.org/0000-0002-4435-4623
A. N. Bender https://orcid.org/0000-0001-5868-0748
B. A. Benson https://orcid.org/0000-0002-5108-6823
D. Dutcher https://orcid.org/0000-0002-9962-2058
A. Foster https://orcid.org/0000-0002-7145-1824
A. Rahlin https://orcid.org/0000-0003-3953-1776
M. Archipley https://orcid.org/0000-0002-0517-9842
J. E. Austermann https://orcid.org/0000-0002-6338-0069
L. Balkenhol https://orcid.org/0000-0001-6899-1873
F. Bianchini https://orcid.org/0000-0003-4847-3483
L. E. Bleem https://orcid.org/0000-0001-7665-5079
F. R. Bouchet https://orcid.org/0000-0002-8051-2924
J. E. Carlstrom https://orcid.org/0000-0002-2044-7665
C. L. Chang https://orcid.org/0000-0002-6311-0448
J.-F. Cliche https://orcid.org/0000-0001-6509-8430
T. M. Crawford https://orcid.org/0000-0001-9000-5013
M. A. Dobbs https://orcid.org/0000-0001-7166-6422
W. Everett https://orcid.org/0000-0002-5370-6651
J. Fu https://orcid.org/0000-0002-3767-299X
R. Gualtieri https://orcid.org/0000-0003-4245-2315
S. Guns https://orcid.org/0000-0001-7143-2853
N. Gupta https://orcid.org/0000-0001-7652-9451
E. Hivon https://orcid.org/0000-0003-1880-2733
G. P. Holder https://orcid.org/0000-0002-0463-6394
A. M. Kofman https://orcid.org/0000-0001-5374-1767
A. T. Lee https://orcid.org/0000-0003-3106-3218
M. Millea https://orcid.org/0000-0001-7317-0551
C. L. Reichardt https://orcid.org/0000-0003-2226-9169
D. Riebel https://orcid.org/0000-0002-4773-2204
B. Riedel https://orcid.org/0000-0002-9524-8943
A. A. Stark https://orcid.org/0000-0002-2718-9996
C. Umilta https://orcid.org/0000-0002-6805-6188
K. Vanderlinde https://orcid.org/0000-0003-4535-9378
J. D. Vieira https://orcid.org/0000-0001-7192-3871
N. Whitehorn https://orcid.org/0000-0002-3157-0407
W. L. K. Wu https://orcid.org/0000-0001-5411-6920

References

Abazajian, K. N., Adshead, P., Ahmed, Z., et al. 2016, arXiv:1610.02743
Ade, P. A. R., Pisano, G., Tucker, C., & Weaver, S. 2006, Proc. SPIE, 6275, 62750U
Ahmed, Z., Amiri, M., Benton, S. J., et al. 2014, Proc. SPIE, 9153, 91531N
Anderson, A. J., Ade, P. A. R., Ahmed, Z., et al. 2020, JLTP, 199, 320
Austermann, J. E., Aird, K. A., Beall, J. A., et al. 2012, Proc. SPIE, 8452, 84521E
Avva, J. S., Ade, P. A. R., Ahmed, Z., et al. 2018, JLTP, 193, 547
Balkenhol, L., Dutcher, D., Ade, P. A. R., et al. 2021, PhRvD, 104, 083509
Bandura, K., Bender, A. N., Cliche, J. F., et al. 2016, JAI, 5, 1641005
BICEP/Keck, Ade, P. A. R., Ahmed, Z., et al. 2021, PhRvD, 103, 042002
BICEP 2 Collaboration, Keck Array Collaboration, Ade, P. A. R., et al. 2017, PhRvD, 96, 102003
BICEP 2 Collaboration, Keck Array Collaboration, Ade, P. A. R., et al. 2018, PhRvL, 121, 221301
BICEP/Keck Collaboration, SPT pol Collaboration, Ade, P. A. R., et al. 2021, PhRvD, 103, 022004
Bender, A. N., Ade, P. A. R., Ahmed, Z., et al. 2018, Proc. SPIE, 10708, 1070803
Bender, A. N., Ade, P. A. R., Anderson, A. J., et al. 2016, Proc. SPIE, 9914, 99141D
Bender, A. N., Anderson, A. J., Avva, J. S., et al. 2020, JLTP, 199, 182
Bender, A. N., Cliche, J.-F., de Haan, T., et al. 2014, Proc. SPIE, 9153, 91531A
Bhatia, R., Chase, S., Edgington, S., et al. 2000, Cryo, 40, 685
Bianchini, F., Wu, W. L. K., Ade, P. A. R., et al. 2020a, ApJ, 888, 119
Bianchini, F., Wu, W. L. K., Ade, P. A. R., et al. 2020b, PhRvD, 102, 083504
Bleem, L. E., Bocquet, S., Stalder, B., et al. 2020, ApJS, 247, 25
Bocquet, S., Dietrich, J. P., Schrabback, T., et al. 2019, ApJ, 878, 55
Carlstrom, J. E., Ade, P. A. R., Aird, K. A., et al. 2011, PASP, 123, 568
Carter, F. W., Ade, P. A. R., Ahmed, Z., et al. 2018, JLTP, 193, 695
Choi, J., Ishitsuka, H., Mima, S., et al. 2013, RScI, 84, 114502
Choi, S. K., Hasselfield, M., Ho, S.-P. P., et al. 2020, JCAP, 2020, 045
Coble, K., Ade, P. A. R., Bock, J. J., et al. 2003, arXiv:astro-ph/0301599
de Haan, T., Smecher, G., & Dobbs, M. 2012, Proc. SPIE, 8452, 84520E
Ding, J., Ade, P. A. R., Ahmed, Z., et al. 2018, JLTP, 193, 712
Dobbs, M. A., Lueker, M., Aird, K. A., et al. 2012, RScI, 83, 073113
Doriese, W., Morgan, K., Bennett, D., et al. 2015, JLTP, 184, 389
Dutcher, D., Ade, P. A. R., Ahmed, Z., et al. 2018, Proc. SPIE, 10708, 107081Z
Dutcher, D., Balkenhol, L., Ade, P. A. R., et al. 2021, PhRvD, 104, 022003
Edwards, J., O'Brient, R., Lee, A., & Rebeiz, G. M. 2012, ITAP, 60, 4082
Everett, W. B., Zhang, L., Crawford, T. M., et al. 2020, ApJ, 900, 55
Galitzki, N., Ali, A., Arnold, K. S., et al. 2018, Proc. SPIE, 10708, 1070804
Galli, S., Benabed, K., Bouchet, F., et al. 2014, PhRvD, 90, 063504
George, E. M., Ade, P., Aird, K. A., et al. 2012, Proc. SPIE, 8452, 84521F
Gralla, M. B., Marriage, T. A., Addison, G., et al. 2020, ApJ, 893, 104
Grant, W. S., & Voorhies, R. 2017, cereal - A C++11 library for serialization, GitHub, https://uscilab.github.io/cereal/
Guns, S., Foster, A., Daley, C., et al. 2021, ApJ, 916, 98
Hasselfield, M., Hilton, M., Marriage, T. A., et al. 2013, JCAP, 2013, 008
Henning, J. W., Sayre, J. T., Reichardt, C. L., et al. 2018, ApJ, 852, 97
Hilton, M., Sifón, C., Naess, S., et al. 2021, ApJS, 253, 3
Hinshaw, G., Larson, D., Komatsu, E., et al. 2013, ApJS, 208, 19
Hu, W., & White, M. 1997, NewA, 2, 323
Huang, N., Bleem, L. E., Stalder, B., et al. 2020, AJ, 159, 110
Hunter, J. D. 2007, CSE, 9, 90
Irwin, K., & Hilton, G. 2005, Transition-Edge Sensors (Berlin: Springer), 63
Jones, E., Oliphant, T., Peterson, P., et al. 2001, SciPy: Open Source Scientific Tools for Python, http://www.scipy.org/
Kamionkowski, M., Kosowsky, A., & Stebbins, A. 1997, PhRvL, 78, 2058
Kamionkowski, M., & Kovetz, E. D. 2016, ARA&A, 54, 227
Kang, J. H., Ade, P. A. R., Ahmed, Z., et al. 2018, Proc. SPIE, 10708, 107082N
Keisler, R., Reichardt, C. L., Aird, K. A., et al. 2011, ApJ, 743, 28
McKinney, W. 2010, Proc. 9th Python in Science Conf., ed. S. van der Walt & J. Millman, 51
Mocanu, L. M., Crawford, T. M., Aylor, K., et al. 2019, JCAP, 2019, 038
Moncelsi, L., Ade, P. A. R., Ahmed, Z., et al. 2020, Proc. SPIE, 11453, 1145314
Montgomery, J. 2021, PhD thesis, McGill Univ.
Montgomery, J., Ade, P. A. R., Ahmed, Z., et al. 2021, arXiv:2103.16017
Nadolski, A., Vieira, J. D., Sobrin, J. A., et al. 2020, ApOpt, 59, 3285
Nadolski, A. W. 2020, PhD thesis, Univ. Illinois at Urbana-Champaign

Naess, S., Battaglia, N., Bond, J. R., et al. 2021, ApJ, 915, 14
Namikawa, T., Guan, Y., Darwish, O., et al. 2020, PhRvD, 101, 083527
Newville, M., Stensitzki, T., Allen, D. B., & Ingargiola, A. 2014, lmfit/lmfit-py: v1.0.3, Zenodo, doi:10.5281/zenodo.5570790
O'Brient, R., Ade, P., Arnold, K., et al. 2010, Proc. SPIE, 7741, 77410J
Padin, S., Staniszewski, Z., Keisler, R., et al. 2008, ApOpt, 47, 4418
Paine, S. 2019, The am Atmospheric Model, v11.0, Zenodo, doi:10.5281/zenodo.3406483
Pan, Z., Ade, P. A. R., Ahmed, Z., et al. 2018, JLTP, 193, 305
Pan, Z., Liu, M., Basu Thakur, R., et al. 2019, ApOpt, 58, 6257
Perez, F., & Granger, B. E. 2007, CSE, 9, 21
Planck Collaboration, Adam, R., Ade, P. A. R., et al. 2016a, A&A, 594, A10
Planck Collaboration, Ade, P. A. R., Aghanim, N., et al. 2016b, A&A, 594, A24
Planck Collaboration, Ade, P. A. R., Aghanim, N., et al. 2016c, A&A, 594, A26
Planck Collaboration, Aghanim, N., Akrami, Y., et al. 2020, A&A, 641, A6
Posada, C. M., Ade, P. A. R., Ahmed, Z., et al. 2015, SuScT, 28, 094002
Posada, C. M., Ade, P. A. R., Ahmed, Z., et al. 2018, JLTP, 193, 703
Radford, S. J., & Holdaway, M. A. 1998, Proc. SPIE, 3357, 486
Radford, S. J. E. 2011, RMxAC, 41, 87
Raguin, D. H., & Morris, G. M. 1993, ApOpt, 32, 2582
Reichardt, C. L., Patil, S., Ade, P. A. R., et al. 2021, ApJ, 908, 199
Runyan, M. C., & Jones, W. C. 2008, Cryo, 48, 448
Schroder, A., Murk, A., Yagoubov, P., & Patt, F. 2016, ITTST, 6, 156
Sherwin, B. D., van Engelen, A., Sehgal, N., et al. 2017, PhRvD, 95, 123529
Sobrin, J. A., Ade, P. A. R., Ahmed, Z., et al. 2018, Proc. SPIE, 10708, 107081H
SPT-3G Collaboration 2019, spt3g_software, GitHub, https://github.com/CMB-S4/spt3g_software
Staniszewski, Z. 2010, PhD thesis, Case Western Reserve Univ.
Stark, A. A. 2018, arXiv:1809.08212
Stiehl, G. M., Cho, H. M., Hilton, G. C., et al. 2011, ITAS, 21, 298
Story, K., Leitch, E., Ade, P., et al. 2012, Proc. SPIE, 8451, 84510T
Suzuki, A., Ade, P., Akiba, Y., et al. 2016, JLTP, 184, 805
Suzuki, A., Ade, P. A. R., Akiba, Y., et al. 2018, JLTP, 193, 1048
Suzuki, A., Arnold, K., Edwards, J., et al. 2012, JLTP, 167, 852
van der Walt, S., Colbert, S. C., & Varoquaux, G. 2011, CSE, 13, 22
Whitehorn, N., Natoli, T., Ade, P. A. R., et al. 2016, ApJ, 830, 143
Wu, W. L. K., Mocanu, L. M., Ade, P. A. R., et al. 2019, ApJ, 884, 70
Zaldarriaga, M., & Seljak, U. 1997, PhRvD, 55, 1830